

The following text is provided by DuEPublico, the central repository of the University Duisburg-Essen.

This version of the e-publication released on DuEPublico may differ from a potential published print or online version.

**Nguyen, Minh Thuong; Proch, Fabian; Wlokas, Irenäus; Kempf, Andreas:**

**Large eddy simulation of an internal combustion engine using an efficient immersed boundary technique**

DOI: <http://dx.doi.org/10.1007/s10494-015-9683-4>

URN: <urn:nbn:de:hbz:464-20170504-114037-3>

Link: <http://duepublico.uni-duisburg-essen.de/servlets/DocumentServlet?id=42245>

Legal notice:

The final publication is available at Springer via <http://dx.doi.org/10.1007/s10494-015-9683-4>

Source: Flow Turbulence Combust (2016) 97: 191; First Online: 11 December 2015

NOTICE: this is the authors version of a work that was accepted for publication in Flow Turbulence and Combustion. Changes resulting from the publishing process, such as peer review, editing, corrections, structural formatting, and other quality control mechanisms may not be reflected in this document. Changes may have been made to this work since it was submitted for publication. A definitive version was subsequently published in Flow, Turbulence and Combustion. <http://link.springer.com/article/10.1007/s10494-015-9683-4>

**Name manuscript No.**  
(will be inserted by the editor)

---

## Large eddy simulation of an internal combustion engine using an efficient immersed boundary technique

T.M. Nguyen · F. Proch · I. Wlokas ·  
A.M. Kempf

Received: date / Accepted: date

**Abstract** This paper presents highly resolved large eddy simulations (LES) of an internal combustion engine (ICE) using an immersed boundary method (IBM), which can describe moving and stationary boundaries in a simple and efficient manner. In this novel approach, the motion of the valves and the piston is modeled by Lagrangian particles, whilst the stationary parts of the engine are described by a computationally efficient IBM. The proposed mesh-free technique of boundary representation is simple for parallelization and suitable for high performance computing (HPC). To demonstrate the method, LES results are presented for the flow and the combustion in an internal combustion engine. The Favre-filtered Navier-Stokes equations are solved for a compressible flow employing a finite volume method on Cartesian grids. Non-reflecting boundary conditions are applied at the intake and the exhaust ports.

---

T.M. Nguyen, F. Proch, I. Wlokas, A.M. Kempf  
Institute for Combustion and Gasdynamics (IVG), Chair for Fluid Dynamics, University of  
Duisburg-Essen, 47057 Duisburg, Germany  
Tel.: +49-(0)203-3798107  
Fax: +49-(0)203-3798102  
E-mail: nguyen.thuong@uni-due.due

Combustion is described using a flame surface density (FSD) model with an algebraic reaction rate closure. A simplified engine with a fixed axisymmetric valve (see Appendix A) is employed to show the correctness of the method while avoiding the uncertainties which may be induced by the complex engine geometry. Three test-cases using a real engine geometry are investigated on different grids to evaluate the impact of the cell size and the filter width. The simulation results are compared against the experimental data. A good overall agreement was found between the measurements and the simulation data. The presented method has particular advantages in the efficient generation of the grid, high resolution and low numerical dissipation throughout the domain and an excellent suitability for massively parallel simulations.

**Keywords** IC Engine · Large Eddy Simulation · Flame Surface Density · Immersed Boundaries · Lagrangian Particles

## 1 Introduction

Large eddy simulations are well suited for the investigation of the physical phenomena inside internal combustion engines with high demands for spatial and temporal accuracy [7]. Early applications of LES to non-premixed [27, 43, 44] and premixed [8, 18, 44] flames demonstrated the capability of LES in combustion modeling. The method has been extended and modified for the modeling of gas turbine combustors [5, 11, 29], spray combustion [1, 50, 51] and coal combustion [12, 17, 64].

In the past, LES was used for modeling of the gas exchange [13, 23] as well as the combustion process inside IC engines [48], utilizing a flame surface density model. Further LES investigations were performed to analyze the fuel-air mixing [52], knock tendency [15], turbulent heat transfer [61] as well as cyclic variations [21, 58].

The aim of the present work is to demonstrate the applicability of a novel approach based on immersed boundaries [41] for the LES of IC engines, which focuses on high numerical efficiency and parallel scalability on modern computer hardware architectures.

To generate meshes for complex geometries, Peskin [41] proposed a novel IBM based on Cartesian grids as a simple and efficient alternative to body-fitted grids. Based on Peskin's approach, different techniques have been developed for further improvement of the IBM in various applications. Numerous approaches of IBM can be categorized based on the numerical treatments of boundary forcing functions or based on the boundary types such as elastic or rigid. More information about IBMs can be found in the review paper of Mitall et al. [33], in which the methodologies, the advantages and the disadvantages of various IBMs are analyzed in a great detail. In this section, we focus our attention on the best known approaches. Goldstein et al. [20] introduced a surface body force as a function of velocity, time and two model parameters ( $\alpha$  and  $\beta$ ). This force represents the feedback force which is induced by the flow velocities on the immersed boundaries. In an approach of Verzicco et al.

[59], suitable body forces are prescribed to yield the desired velocity on a given surface. The technique is simple, computational efficient, and flexible even in complex geometries.

A similar approach using an external force field was proposed by Balaras [2]. Utilizing the detailed topology description of the boundary to distribute the surface force properly, this methodology provides a highly accurate interface tracking scheme between fluid and solid regions and hence reduces the complexity related to the computation of the sub-grid fluxes in the solid interface's vicinity. This approach is well-suited for stationary immersed boundaries but lacks the proper treatment of moving boundaries where the interfaces between fluid and solid are a function of time and space. According to the Goldstein's assumption [20], the computational overhead is due to the increasing number of iterations for the desired constants  $\alpha$  and  $\beta$  since the fluid-solid interface is time-dependent. The improved method of Balaras also introduces a large overhead which has been a standing problem for the community since a significant computational effort is required for the solid-fluid interface tracking with a second order accuracy scheme. Furthermore, as the B-splines method [35] is used for interface tracking, the moving boundary leads to grid restructuring, which makes the approach more expensive. Tullio et al. [54] developed an IBM for compressible flows using a flexible local refinement technique to resolve the flow near the immersed body. The method is second-order accurate and can solve complex flows on a non-uniform Cartesian grid with a low computational cost compared to the corresponding fine equidistant Cartesian grid. However, applying this approach to the moving boundary would be problematic since the complicated grid with local refinement has to be regenerated frequently during the simulation. In the IBM proposed by Taira et al. [53], the pressure and boundary force are regarded as Lagrange multipliers required to maintain the divergence-free and the no-slip conditions. The boundary force is determined implicitly by a projection, in which the slip and non-divergence-free components of the velocity field are removed. This method is well-suited for both stationary and moving boundaries.

In the work of Udaykumar et al. [57], a mixed Eulerian-Lagrangian method is used to simulate the flow and geometries with complex and moving boundaries. Lagrangian particles are translated explicitly as a marker for the position and the shape of the boundaries, the governing equations are solved on an Eulerian grid. A straightforward method proposed by Mittal et al. [34] combines the cell blanking approach and the arbitrary Lagrangian-Eulerian method [25] by using two independent meshes: the stationary mesh and the moving mesh. The intersection between the moving grid and the fixed grid is calculated for the solid-fluid interfaces, allowing flexible mesh generation. However, dealing with mesh intersections between the fixed grid and the moving grid makes this method more complicated and computationally expensive. Forrer et al. [16] proposed the concept of 'mirror flow', in which the values of the cells inside the interior of a moving object are extrapolated from a given solution. This approach is developed to solve the compressible, time-dependent Euler equations on a Cartesian grid with stationary and moving walls. Our proposed

IB technique in this paper is mainly based on this concept of ‘mirror flow’. Since it was shown that the concept of ‘mirror flow’ is well-suited for hyperbolic problems [16], we applied it for the solution of the filtered compressible Navier-Stokes equations with moving boundaries.

In our approach, a structured grid is used throughout the whole computational domain in which the immersed boundary technique [41] is applied. Since the geometry description depends on the resolution of the Cartesian grid, the geometrical features which are smaller than a grid cell ( $\Delta$ ) can not be resolved. The geometry description on an uniform Cartesian grid is automatically generated from the STL representation of the geometry of the engine within minutes without further user interaction. To avoid the complexity of the mesh motion, a meshfree technique is applied to model the moving parts of the simulated engine: the piston and the valves are represented by different groups of Lagrangian particles with corresponding motion functions. To be more precise, this technique employs the moving objects in two forms: Lagrangian particles and immersed boundaries. The Lagrangian form is utilized to handle the motion of the objects in the computational domain while the immersed boundary form is employed to impose the flow condition at the moving boundaries using the ‘mirror flow’ concept by Forrer et al. [16]. By blocking the computational cells that belong to the solid parts (where Lagrangian particles are located), no mesh alteration or new mesh is required during the simulation. The parallelization is highly efficient due to the fact that the domain decomposition is independent from the engine geometry.

The numerical and physical boundary conditions at the intake and exhaust ports are obtained by solving the system of equations for non-reflecting boundary conditions [46]. The combustion modeling in the power stroke is performed with a flame surface density model. In our opinion, an uniformly high resolution of the entire in-cylinder region is required (not just the near wall regions) to avoid artificial dissipation of the turbulent structures, which is a prerequisite to describe the flame front propagation accurately. Alternatively, adaptive grid refinement of the flame front may not circumvent well the issue of artificially dissipated turbulent structures and makes the computation rather complicated, expensive and possibly less reproducible. Figure 1 illustrates the instantaneous turbulent flow field and the fine structures that are resolved during an engine LES.

## 2 Modeling Approach

### 2.1 The governing equations

The filtered governing equations for mass (1), momentum (2), and energy (3) are outlined below.

$$\frac{\partial \bar{\rho}}{\partial t} + \frac{\partial \bar{\rho} \tilde{u}_j}{\partial x_j} = 0 \quad (1)$$

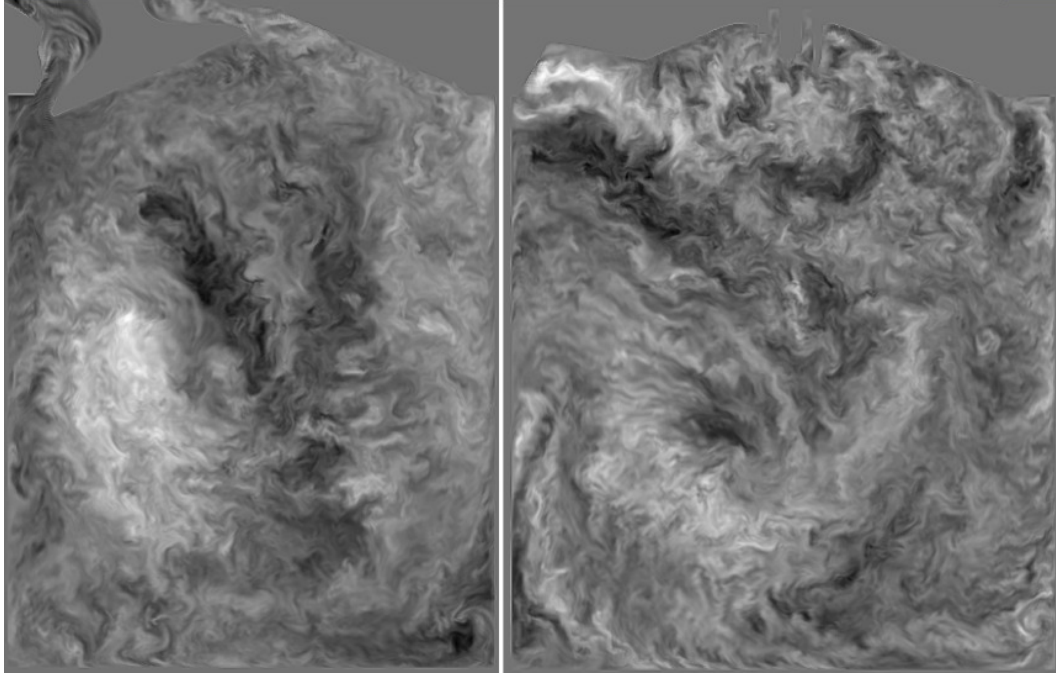


**Fig. 1** Instantaneous image-normal velocity component in the valve section (left) and in the tumble-symmetry plane (right) obtained from LES with a domain size of 180 million cells, each pixel corresponds to one computational cell with an edge length of 0.2 mm

$$\begin{aligned}
 & \frac{\partial \bar{\rho} \tilde{u}_i}{\partial t} + \frac{\partial \bar{\rho} \tilde{u}_j \tilde{u}_i}{\partial x_j} = - \frac{\partial \bar{p}}{\partial x_i} \\
 & + \frac{\partial}{\partial x_j} \left[ \bar{\rho} \tilde{\nu} \left( \frac{\partial \tilde{u}_i}{\partial x_j} + \frac{\partial \tilde{u}_j}{\partial x_i} \right) - \frac{2}{3} \bar{\rho} \tilde{\nu} \frac{\partial \tilde{u}_k}{\partial x_k} \delta_{ij} - \bar{\rho} \tau_{ij}^{sgs} \right]
 \end{aligned} \tag{2}$$

$$\begin{aligned}
 & \frac{\partial \bar{\rho} \tilde{e}}{\partial t} + \frac{\partial (\bar{\rho} \tilde{e}) \tilde{u}_j}{\partial x_j} = \bar{w}_T + \frac{\partial}{\partial x_j} \left( \kappa \frac{\partial \tilde{T}}{\partial x_j} \right) \\
 & + \frac{\partial}{\partial x_j} \left( \tilde{u}_i \tilde{\sigma}_{ij} \right) - \frac{\partial}{\partial x_j} \left( \kappa_{ij}^{sgs} \right)
 \end{aligned} \tag{3}$$

In Eqs. (1-3), the density, velocity, pressure, molecular viscosity and Kronecker delta are denoted by  $\bar{\rho}$ ,  $\tilde{u}_i$ ,  $\bar{p}$ ,  $\tilde{\nu}$  and  $\delta_{ij}$ , respectively. The unresolved stress and the unresolved kinetic energy are  $\tau_{ij}^{sgs}$  and  $\kappa_{ij}^{sgs}$ . The total energy, Cauchy stress tensor and the temperature are represented by  $\tilde{e}$ ,  $\tilde{\sigma}_{ij}$  and  $\tilde{T}$ , respectively.

The equation of state of an ideal gas is given in Eq. 4:

$$p = \rho RT, c_v = \frac{R}{\gamma - 1}, c_p = c_v + R \quad (4)$$

The gas constant, the heat capacity at constant volume and pressure are represented by  $R$ ,  $c_v$  and  $c_p$ , respectively.

The total internal energy  $\tilde{e}$  and the sensible internal energy  $\tilde{e}_s$  are determined according to Eq. 5 (Poinsot and Veynante [45]).

$$\bar{\rho}\tilde{e} = \frac{1}{2}\bar{\rho}\tilde{u}_k\tilde{u}_k + \bar{\rho}\tilde{e}_s, \quad \tilde{e}_s = \int_{T_0}^T c_v(T) dT \quad (5)$$

The combustion modeling of this study is discussed in section 2.6. For the investigated test cases, the air and the fuel are assumed to be perfectly mixed and hence no additional transport equation is needed to describe the composition of the mixture. The heat release due to combustion is computed by  $\bar{w}_T = \sum_{k=1}^n \Delta h_{f,k}^o \dot{\omega}_k$  as the product of the formation enthalpy  $\Delta h_{f,k}^o$  of species  $k$  and the reaction rate  $\dot{\omega}_k$ .

## 2.2 From moving boundaries to Lagrangian particles

The moving boundaries are numerically described by Lagrangian particles, which must be generated prior to the simulation using available software for "voxelization" (voxel: volume element). In our approach, the voxelization step must be carried out first to convert a geometric object (the moving object) into a set of voxels with the resolution of the computational domain. Obviously the number of voxels describing any moving geometries depends on the resolution of the computational grid. This set of voxels is then mapped onto the main computational grid for correct positioning. By then, the indices of each voxel in the computational domain will be assigned to a Lagrangian particle's index and the initial coordinate of a particle can be computed from its indices. Figure 2 illustrates the basic steps to generate Lagrangian particles from the original geometry. By using Lagrangian particles for the description of the moving parts, the motion of these objects is characterized as the motion of the individual particles in a Lagrangian manner. Therefore, the transport equations for the individual particles in space and time must be considered. Generally, based on the particle velocity  $v_{pi}$  and the location  $x_i^{\text{old}}$  from the last time step, the new location  $x_i^{\text{new}}$  is calculated according to Eq. 6.

$$x_i^{\text{new}} = x_i^{\text{old}} + v_{pi}^{\text{old}} \Delta t \quad (6)$$

The motion of the piston, the intake and exhaust valves are determined as a function of the crank angle. From the valve lift profiles, the velocity  $v_{pi}$

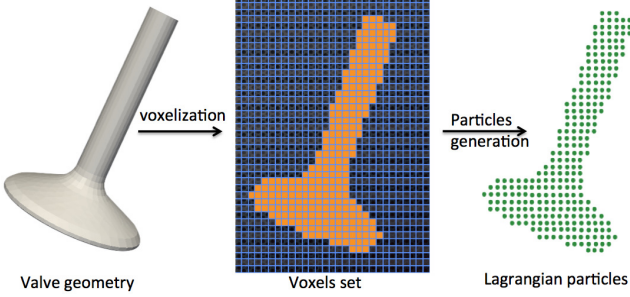


**Fig. 2** Two-step procedure to generate Lagrangian particles from the original geometry. First, voxelization converts a geometric object into a set of voxels, then, a particle is created from each voxel

and acceleration  $a_{pi}$  of the group of the particles describing the intake or the exhaust valves are calculated from Eqs. 7-8.

$$v_{pi} = \frac{x_i^{\text{new}} - x_i^{\text{old}}}{\Delta t} \quad (7)$$

$$a_{pi} = \frac{v_{pi}^{\text{new}} - v_{pi}^{\text{old}}}{\Delta t} \quad (8)$$

In contrast to the valve particles, the motion of the piston particles is modeled in a simpler manner since the piston velocity and the piston acceleration can be analytically calculated from the piston kinematics based on the crank angle (CA)  $\Theta$ , the conrod length  $l$ , the crank radius  $r$ , and from the angular velocity  $\omega$  ( $\omega = 2\pi \text{ rpm} / 60$ ) from Eqs. 9-10 [24]. These simplified equations (no offset of the piston) are sufficient since there is no such offset in the experiment.

$$v_{pi} = \left[ -r \sin \Theta - \frac{r^2 \sin \Theta \cos \Theta}{\sqrt{l^2 - r^2 \sin^2 \Theta}} \right] \omega \quad (9)$$

$$a_{pi} = \left[ -r \cos \Theta - \frac{r^2 (\cos^2 \Theta - \sin^2 \Theta)}{\sqrt{l^2 - r^2 \sin^2 \Theta}} \right. \\ \left. - \frac{r^4 (\cos^2 \Theta \sin^2 \Theta)}{\sqrt{l^2 - r^2 \sin^2 \Theta}} \right] \omega \quad (10)$$

Besides the actual particle positions  $x_i$ , the logical particle coordinates  $(i,j,k)$  within the grid must be computed from the actual position  $x_i$  and the cell size  $\Delta$ , considering  $nG$  layers of ghost cells that may be used around the computational domain. For the isotropic and  $(i,j,k)$  countable computational grid (Cartesian grids) used in our approach, this is achieved by following Eq. 11.

$$i = \left\lfloor \frac{x_i}{\Delta} \right\rfloor + 1 + nG \quad (11)$$

After transporting the particles to the new position in the computational domain, the cell-blocking procedure is performed to establish the new interface between fluid and solid regions. This step is executed by introducing an immersed boundary field (IBF) as the partition of fluid and solid zones. Taking full advantage of the equidistant Cartesian grid, the blocking of solid cells can be done simply by using the calculated indices  $i,j,k$  of the corresponding cell where a particle is located:

$$\text{IBF}_{i,j,k} = 0 \quad (12)$$

### 2.3 Impose boundary conditions at the moving boundaries

In order to include the effect of the moving boundaries on the surrounding fluid, most of the aforementioned approaches (see section 1) introduced a forcing function  $\mathbf{f}_b$  and then modified the equation system  $L(\Phi) = 0$  to the new one  $L(\Phi) = \mathbf{f}_b$ , accordingly ( $\Phi$  is the vector of conservative variables). The forcing function can be included into the governing equations before (continuous forcing approach) or after (discrete forcing approach) discretization [33]. An iterative calculation must be carried out to obtain this forcing function for the flow around a rigid body.

Instead of introducing a forcing function  $\mathbf{f}_b$ , in our approach, the effect of the moving boundaries  $\Gamma_b$  on the surrounding fluid is included via the ‘mirror flow’ concept [16]. The discretized governing equations are modified by imposing the ‘mirror flow’ quantities  $\Phi_T$  inside the immersed boundaries  $\Gamma_b$ . These ‘mirror’ quantities  $\Phi_T$  are extrapolated from neighboring fluid cells and from the particle properties, so that the flow conditions at the moving boundaries are imposed correctly.

The procedure is as follows: after solving the discretized Navier-Stokes equations  $L(\Phi) = \mathbf{0}$  for the numerical solutions  $\Phi^n$  at time step  $t_n$ , the ‘mirror flow’ quantities  $\Phi_T$  of the solid cells inside the moving boundaries  $\Gamma_b$  are calculated based on the predetermined particle’s properties ( $v_{pi}^{n+1}$  and  $a_{pi}^{n+1}$ ) at time step  $t_{n+1}$  and the data extrapolated from the neighboring fluid cells  $\Phi^n$ . Afterward, the discretized Navier-Stokes equations are solved for the numerical solution  $\Phi^{n+1}$  in the whole computational domain. In other words, the explicit time-stepping is performed with the moving boundary positions from the time step  $t_{n+1}$  before advancing the whole numerical solution to the next time step  $t_{n+1}$ .

The imposed velocities  $v_{si}$  of the solid cells at the solid-fluid interfaces are computed from the particle’s velocity  $v_{pi}$  and the velocity  $v_{fi}$  of the neighbor-

ing fluid cells  $N_{nb}$ :

$$v_{si} = 2v_{pi} - \frac{\sum_{j=1}^{N_{nb}} v_{fij}}{N_{nb}} \quad (13)$$

Following Forrer et al. [16], the pressure gradient  $\partial p / \partial x_i$  of a boundary cell is calculated from the corresponding particle's acceleration  $a_{pi}$  and the averaged density  $\rho_j$  of the neighboring fluid cells:

$$\frac{\partial p}{\partial x_i} = -\frac{\sum_{j=1}^{N_{nb}} \rho_j}{N_{nb}} a_{pi} \quad (14)$$

To be more specific, the numerical quantities of a solid cell at the boundary require averaged quantities from the neighboring fluid cells  $N_{nb}$  where  $0 \leq N_{nb} \leq 6$ .

Since the pressure  $p$  and the velocities of the solid cells  $v_{si}$  are set, the corresponding energy  $e_{si}$  is also required to account for the kinetic energy of the particles' motion as well as the sensible energy of the cylinder wall:

$$e_{si} = \frac{1}{2} v_{si}^2 + c_v T_{si} \quad (15)$$

The heat flux at the wall boundary is calculated by Fourier's law  $q_i = -\kappa \frac{\partial T}{\partial x_i}$  with the gas thermal conductivity  $\kappa$ . The isothermal boundary condition is used by setting the wall temperature to a fixed value. Due to the lack of experimental data, the temperature at the moving boundaries is set to the same value as the wall temperature  $T_{wall}$  of the cylinder. In the current work, we do not use any additional modeling of wall heat transfer - a known and difficult problem for engine LES.

## 2.4 Closing and opening the valves

The valve gap during simulation can only be resolved up to a certain valve lift value depending on the grid resolution. In order to close the valves, all the computational cells in the gap (the smallest resolved valve lift) between the valves and the wall are blocked ( $IBF_{ijk} = 0$ ), so that preventing the fluid escaping out of the cylinder.

In order to reopen the valves, the blocked cells in the gap between the valve and the wall are unblocked (the  $IBF$  value is changed from 0 to 1). Since these freshly cleared cells (the cells, which were solid at time step  $t_n$ , become the fluid cells at time step  $t_{n+1}$ ) have no fluid history, it is important to fill these cells with the flow data (velocity, density, temperature and pressure) by interpolating the data from neighboring fluid cells. Alternatively, a simple one-dimensional interpolation operation proposed by Udaykumar et al. [56] can be used to fill the freshly cleared cells with the flow data.

## 2.5 The intake and the exhaust boundary conditions

Based on the measured mass flow and the measured time-dependent pressure, non-reflecting boundary conditions are enforced at the end of the truncated inlet and exhaust ports, which have a length of 60 and 110 mm, respectively. Depending on the amplitude variations of characteristic waves which are entering or leaving the computational domain, the time-dependent physical flow conditions are computed by solving the locally one-dimensional and inviscid (LODI) system as proposed by Poinsot et al. [46]. The obtained values for the density  $\rho$ , velocities  $u_i$ , pressure  $p$  and the energy  $e$  are imposed on the cells at the inlet and the outlet of the domain.

## 2.6 Combustion modeling

The combustion process is modeled with the flame surface density (FSD) approach. The flame propagation is described by the progress variable  $c$ , which is based on the fuel mass fraction  $Y_F$ , where  $Y_F^u$  denotes the unburned and  $Y_F^b$  the burned state ( $Y_F^u = 0$  for lean condition).

$$c = \frac{Y_F - Y_F^u}{Y_F^b - Y_F^u} \quad (16)$$

The transport equation for the Favre-filtered progress variable reads:

$$\begin{aligned} & \frac{\partial \tilde{c}}{\partial t} + \frac{\partial \tilde{\rho} \tilde{c} \tilde{u}_i}{\partial x_i} + \frac{\partial}{\partial x_i} [\bar{\rho}(\tilde{c} \tilde{u}_i - \tilde{c} \tilde{u}_i)] \\ &= \frac{\partial}{\partial x_i} (\bar{\rho} D \frac{\partial c}{\partial x_i}) + \bar{w}_c = \bar{\rho} S_d \Sigma_{\text{gen}} \end{aligned} \quad (17)$$

In this equation, the mean reaction source term and the molecular diffusivity are  $\bar{w}_c$  and  $D$ . The displacement speed and the generalized flame surface density are denoted as  $S_d$  and  $\Sigma_{\text{gen}}$ , where the generalised flame surface density combines molecular diffusion and the source term.

The sub-grid scalar flux and the generalised flame surface density are modeled by Eqs. 18-19.

$$\frac{\partial}{\partial x_i} [\bar{\rho}(\tilde{c} \tilde{u}_i - \tilde{c} \tilde{u}_i)] = \frac{\partial}{\partial x_i} \left( \bar{\rho} \frac{\nu_t}{S_c} \frac{\partial \tilde{c}}{\partial x_i} \right) + F_{cgt} \quad (18)$$

$$\begin{aligned} \bar{\rho} S_d \Sigma_{\text{gen}} &\approx \rho_u S_l \Sigma_{\text{gen}} = \rho_u S_l \Xi |\nabla \bar{c}| - F_{cgt} \\ &\approx \rho_u S_l \Xi |\nabla \tilde{c}| \end{aligned} \quad (19)$$

In these equations, the turbulent viscosity, the turbulent Schmidt number, the laminar flame speed and the wrinkling factor are referred to as  $\nu_t$ ,  $Sc$ ,  $S_l$  and  $\Xi$ , respectively. As it has been shown by Ma et al. [32], the counter gradient transport  $F_{cgt}$  is implicitly modeled by replacing the Reynolds-averaged by

the Favre-averaged progress variable in Eq. 19. The unburned gas density  $\rho_u$  is computed from the ambient pressure and density ( $p_{in}$ ,  $\rho_{in}$ ) as given in Table 2, the heat capacity ratio  $\gamma$  and the actual pressure inside the engine according to Eq. 20.

$$\rho_u = \rho_0 (p/p_0)^{(1/\gamma)} \quad (20)$$

The wrinkling factor is evaluated from the model proposed by Muppala et al. [38] according to Eq. 21, which is preferred here since it considers the effect of the pressure variation on the flame propagation which is important for engine simulations.

$$\Xi = 1 + a \text{Re}_t^{0.25} \left( \frac{u'}{S_l} \right)^b \left( \frac{p}{p_0} \right)^c \quad (21)$$

The turbulent Reynolds number  $\text{Re}_t$  is computed as  $\text{Re}_t = u' \Delta / \nu$  with the cell size  $\Delta$  and the laminar viscosity  $\nu$ . For the iso-octane/air flame, the model parameters are set to  $b = 0.2$ ,  $c = 0.2$ , and  $a = 0.46/\text{Le}$  [24, 38].

The sub-grid scale velocity fluctuation  $u'$  is estimated according to Wyngaard [62]:

$$u' = \sqrt{\frac{2}{3} \kappa_{sgs}}, \quad \kappa_{sgs} = \frac{1}{(C_v \Delta)} \nu_t^2 \quad (22)$$

We chose  $C_v = 0.1$  [28] and  $\nu_t$  is obtained from the Nicoud's  $\sigma$  model [40].

The laminar flame speed can be determined according to Heywood [24]:

$$S_l = S_{l,0} \left( \frac{T_u}{T_0} \right)^\alpha \left( \frac{p}{p_0} \right)^\beta \quad (23)$$

In Eq. 23, the unburned gas temperature  $T_u$  is calculated from  $T_u = T_0 (p/p_0)^{\frac{\gamma-1}{\gamma}}$ . The parameters  $S_{l,0}$ ,  $\alpha$  and  $\beta$  depend on the specific fuel, the equivalence ratio and the burned gas dilution fraction [24]. Wall heat losses were considered to be distributed homogeneously over the combustion chamber by a modified heat capacity ratio of  $\gamma = 1.3$ . This treatment was necessary as a detailed heat transfer modeling would have required an even finer grid resolution or a suitable wall model.

The ignition is created by setting the progress variable  $c$  in a small number of cells near the spark-plug to a value of 1.0 (burned area). The minimum ignition energy that is added to the system and the critical radius of the initial flame kernel are estimated based on the flammability limits [55].

### 3 Experiments

The measurements were performed in a four-stroke optical engine operated in the Dreizler group at Darmstadt University [3], using iso-octane ( $\text{C}_8\text{H}_{18}$ ) as the surrogate fuel. Optical access is provided by a quartz glass cylinder liner

and a flat piston window. The engine features a twin-cam, an overhead-valve pent-roof cylinder head with two intakes and two exhaust valves. A detailed description can be found in Tables 1, 2 and in the paper by Baum et al. [3].

Particle imaging velocimetry (PIV) was applied to capture the flow field within the cylinder. The spatial resolution of the data shown in this paper was 1.8 mm. The engine is motored at 800 rpm and 1500 rpm with a geometric compression ratio of 8.5:1. The measurements were carried out over 2700 and 600 cycles for the cases with 800 and 1500 rpm, respectively. The measurements showing the flame propagation (Fig. 18) were provided by Brian Peterson from Darmstadt University (private communication). High-speed imaging of Mie-scattering of evaporating oil droplets within the reaction zone was used to distinguish between burned and unburned gas regions within a horizontal swirl plane 1.3 mm below the spark plug, similar to the procedure presented in Fansler et al. [14].

| Data                                   | Value                |
|--|----------------------|
| Engine speed                           | 800 rpm & 1500 rpm   |
| Compression ratio                      | 8.5                  |
| Displacement volume                    | 499 cm <sup>3</sup>  |
| Crevice volume                         | 2 cm <sup>3</sup>    |
| Volume at top dead center (TDC)        | 66.5 cm <sup>3</sup> |
| Bore                                   | 86 mm                |
| Stroke                                 | 86 mm                |
| Cylinder clearance height              | 2.6 mm               |
| Intake valve closure (IVC)             | -125 CA              |
| Exhaust valve open (EVO)               | 105 CA               |
| Exhaust valve close (EVC)              | -345 CA              |
| Intake valve open (IVO)                | 325 CA               |
| Avg. pressure intake ( $p_{in}$ )      | 0.95±0.02 bar        |
| Avg. pressure exhaust ( $p_{out}$ )    | 1.00±0.016 bar       |
| Intake temperature ( $T_{in}$ )        | 22.9±0.1°C           |
| Exhaust temperature ( $T_{out}$ )      | 43.7±0.1°C           |
| Mass air in $\langle m_{in} \rangle$   | 11.5 kg/h±2 %        |
| Mass air out $\langle m_{out} \rangle$ | 11.5 kg/h±2 %        |

**Table 1** Engine specifications in the motored case

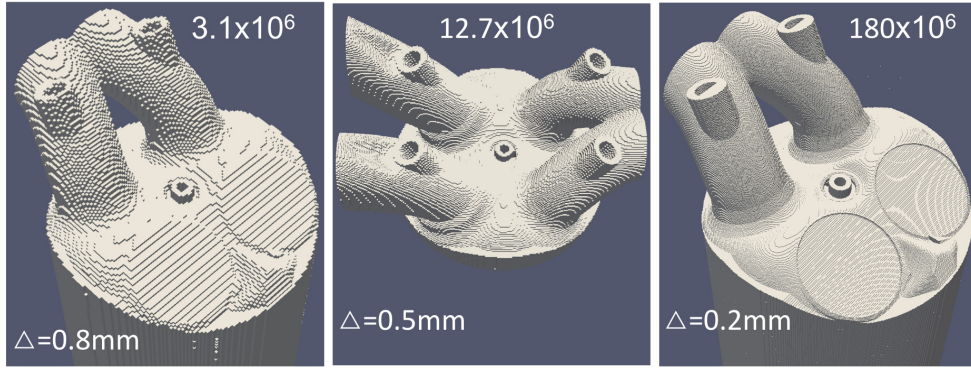
#### 4 Numerical Setup

Simulations were performed on three different grids with cell sizes of 0.8 mm, 0.5 mm and 0.2 mm, as illustrated in Fig. 3. This leads to domains of 3.1, 12.7, and 180 million cells. The computations were performed on 24, 240 and

| Data                              | Value                    |
|-----------------------------------|--------------------------|
| Engine speed                      | 800 rpm                  |
| Compression ratio                 | 8.5                      |
| Spark timing (ST)                 | -16 CA                   |
| Fuel                              | Iso-Octane               |
| Equivalence ratio ( $\phi$ )      | 0.833                    |
| Avg. pressure intake ( $p_{in}$ ) | $0.95 \pm 0.02$ bar      |
| Intake temperature ( $T_{in}$ )   | $47 \pm 3^\circ\text{C}$ |
| Intake density ( $\rho_{in}$ )    | 1.0344 kg/m <sup>3</sup> |

**Table 2** Engine specifications in the combustion case

8196 CPUs, respectively. The ratios between the number of solid cells and the number of fluid cells for different grid sizes when the piston is located at the TDC/BDC are shown in Table 3.

**Fig. 3** The Cartesian grids of the engine geometry in different resolutions ( $\Delta = 0.8$  mm, 0.5 mm, and 0.2 mm)

| Grid              | BDC                                   | TDC                                    |
|-------------------|---------------------------------------|--|
| $\Delta = 0.8$ mm | $1.74 \times 10^6 / 1.36 \times 10^6$ | $2.26 \times 10^6 / 0.84 \times 10^6$  |
| $\Delta = 0.5$ mm | $7.0 \times 10^6 / 5.7 \times 10^6$   | $9.2 \times 10^6 / 3.5 \times 10^6$    |
| $\Delta = 0.2$ mm | $95.4 \times 10^6 / 84.6 \times 10^6$ | $124.6 \times 10^6 / 55.4 \times 10^6$ |

**Table 3** The ratio of the number of the solid cells/fluid cells at TDC and BDC

The LES in-house code PsiPhi [26, 39, 42, 47, 50] was used to solve the Favre-filtered governing equations for a compressible fluid (Eqs. 1-3). The code

uses simple equidistant grids, thus requires more cells for a simulation than an non-uniform grid would, which is often (over)-compensated by the better accuracy and the fact that the computational costs per cell are, in our experience, one to two orders of magnitude lower. A clear advantage of our approach is that the numerical error corresponds exactly to the error of the applied interpolation scheme, while on irregular grids additional terms may appear and contribute to the truncation error. Furthermore, schemes of higher order require on unstructured grids very complicated and large stencils - which is computationally expensive (even though unstructured codes like AVBP [22] and YALES2 [37] demonstrate that 3<sup>rd</sup> order schemes are practicable).

Time integration is performed with an explicit third order Runge-Kutta scheme. Due to temporal accuracy requirements and the limited stability of the explicit time integration scheme, the time step was constrained by the magnitude of the flow velocity  $|u_i|$ , the speed of sound  $a$  and a CFL number of 0.3 according to:

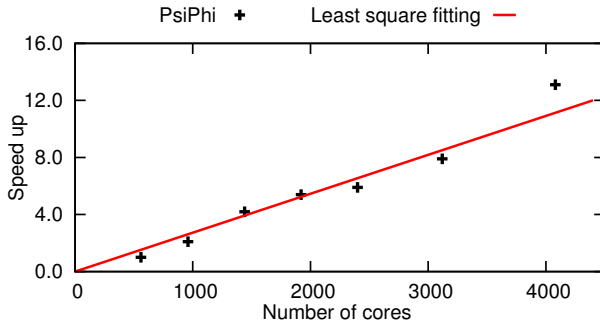
$$\Delta t = 0.3 \frac{\Delta}{|u_i| + a} \quad (24)$$

A second order central differencing scheme is applied for the computation of the momentum fluxes. For density and scalars a total variation diminishing (TVD) scheme with a nonlinear CHARM limiter [63] is used. The unresolved turbulent viscosity is determined with Nicoud's  $\sigma$  model [40, 49], where the model constant  $C_m$  is set to 1.5.

In our method, the numerical operations that solve the ordinary differential equations (ODEs) for the particle transport, block the computational cells (where the particles are located), and enforce the boundary conditions at the moving walls can be performed with a high computational efficiency on parallel machines. The code utilizes the optimized built-in Fortran vectorized field operations on a Cartesian grid. Scalability tests (in Table 4) of PsiPhi on the Cray-XT6m at the University of Duisburg-Essen (Fig. 4) confirm the capability of the approach. In these tests, the cost of transporting particles and enforcing the flow conditions at the moving boundaries is less than 5% although the particles are not equally distributed across parallel domains. Obviously, there is room for improved efficiency but this would affect the simplicity and possibly the speed of the overall simulation: it is not clear if an optimized domain decomposition and particle distribution, with all the resulting overhead, would be really beneficial.

In order to test the performance of our approach in a massively parallel simulation, a test case using more than 180 million cells was computed on the Blue Gene/Q machine JUQUEEN (FZ Juelich through NIC Germany) using 8196 cores. The cost of all the necessary steps (voxelization & particle generation) to produce the input geometry for the simulation was less than one cpu-h. The total number of particles (including intake, exhaust and piston particles) was less than three million even on the finest grid. Although solving the ordinary differential equations must be carried out for all the particles, the operators to enforce the flow conditions at the interface between fluid and solid are only performed using the boundary particles which usually account

| Test case | CPUs (Cartesian topology) | Cells per CPU | Nparticles/Ncells |
|-----------|---------------------------|---------------|-------------------|
| 1         | 560 (10x8x7)              | 1784000       | 0.2%              |
| 2         | 960 (12x10x8)             | 1047230       | 0.2%              |
| 3         | 1440 (15x12x8)            | 694330        | 0.2%              |
| 4         | 1920 (16x12x10)           | 522210        | 0.2%              |
| 5         | 2400 (20x12x10)           | 415740        | 0.2%              |
| 6         | 3120 (20x13x12)           | 319800        | 0.2%              |
| 7         | 4080 (20x17x12)           | 243984        | 0.2%              |

**Table 4** Configurations for scalability test case with PsiPhi**Fig. 4** Strong scaling test on a Cray-XT6m

for 15-30 % of the total particles. Therefore, the total number of numerical operations to handle the moving boundaries in our proposed approach is relatively small, compared to the numerical treatment that is required for solving the Navier-Stokes equation. On the finest grid with 180 million cells and a resolution of 0.2 mm throughout the entire computational domain, to complete the simulation of one full cycle, the total computational cost was around 3.15 millions cpu-h for the motored-case at 1500 rpm.

## 5 Results

### 5.1 Motored-case at 800 rpm

Figure 5 shows a comparison between the velocity magnitude obtained from the simulation on the 0.5 mm grid and the PIV measurements at -270° CA. A fair quantitative agreement between the measured and the simulated velocity structures can be observed. The unsteady nature of the flow field becomes clearly visible as the instantaneous velocity profiles from the medium simulation are plotted along with the mean values in Figs. 6, 7, 12 and 13.

Figures 6 and 7 compare the measured phase averaged velocity against the mean velocities obtained on different grids and 15 instantaneous velocity

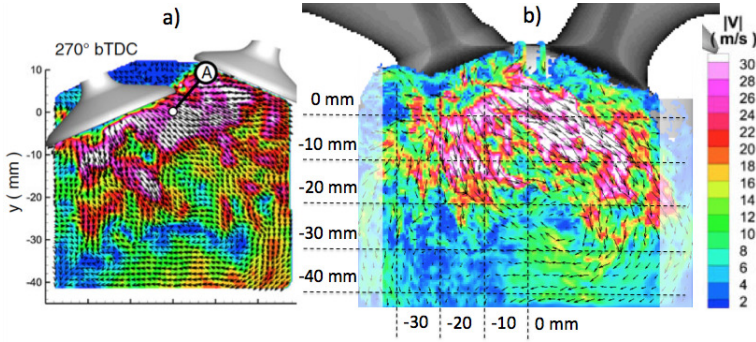


**Fig. 5** Illustration of the instantaneous measured velocity magnitude (a) at  $-270^\circ$  CA (Reprinted from Baum et al. [3] with permission from Springer) and the corresponding velocity magnitude obtained on the medium grid (b) with all the sampling lines

profiles from the medium grid at the sampling lines, shown in Fig. 5, for a crank angle of  $-270^\circ$  CA. Comparisons are shown for the medium and coarse grid, averaged over 15 cycles. Good agreement was observed for all investigated grid resolutions. Even on the coarsest grid (0.8mm) the flow dynamics could be represented correctly. The comparison at  $-270^\circ$ CA in Fig. 6 and Fig. 7 indicates good agreement between the simulations and the experimental data for all the sampling lines, although the horizontal velocity profiles ( $u$ ) at the lines -30mm and -40 mm below the cylinder head (Fig. 6) show some deviation from the corresponding measurements. The differences of the horizontal velocity ( $u$ ) at the aforementioned sampling lines could be likely anticipated since the kinetic energy of the intake flow is strongly dissipated in the downstream region of the cylinder and therefore leads to the relatively small velocities in this area. In the downstream region, where the horizontal velocity component is usually small, a minor disturbance created during the intake could significantly affect the flow velocity in the horizontal direction. Moreover, since the downstream region is close to the piston surface, the boundary layer, which is not well-resolved, may also lead to the deviation between the simulated and the measured data. Along the tumble plane of the cylinder, good agreement between the numerical results and the measurements is achieved for both the coarse (0.8 mm) and the medium (0.5 mm) grid as shown in Fig. 7. For the vertical sampling lines, small discrepancies between the horizontal velocity component ( $u$ ) and the corresponding measured velocity are also found in the downstream region. The similar flow pattern with the distinctive flow structures and vortices is illustrated in Fig. 8, where a good agreement between the simulations and the measurement is achieved. Despite the coarse grid, the results obtained from the simulation ( $\Delta = 0.8$  mm) show a strong resemblance to the measurement since the larger number of engine cycles are converged towards the ensemble-mean flow. A good agreement between the measured and simulated root mean square (RMS) for the two velocity components ( $u,v$ ) is also shown in Figs. 6, 7,

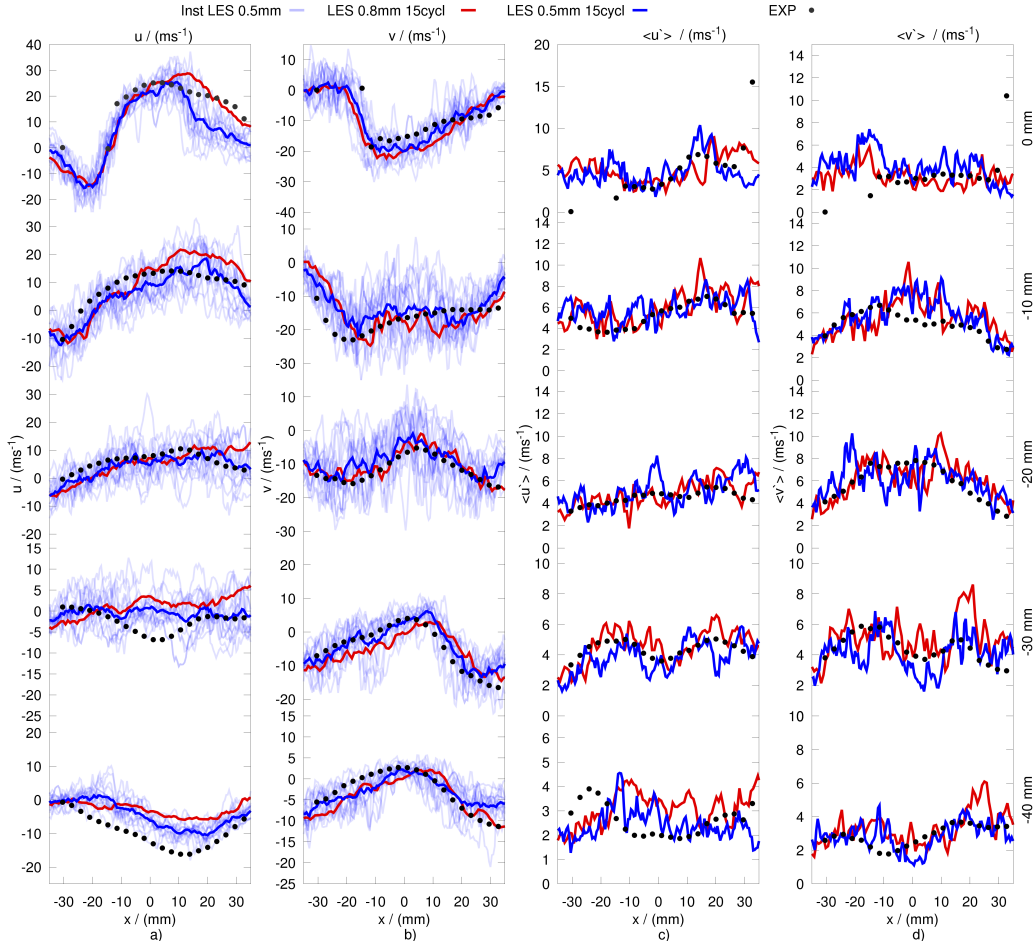


**Fig. 6** Predicted and measured velocity profiles at  $-270^\circ$  CA. Lines in sub-figures (a) and (b) represent the phase averaged horizontal velocity component  $u$  and the vertical velocity component  $v$ . Additionally, 15 instantaneous velocity profiles obtained by the simulation on the medium grid are shown. Sub-figures (c) and (d) illustrate the corresponding RMS of  $u$  and  $v$ , respectively. Experimental results are shown with symbols. Results are shown for the horizontal sampling lines at 0 mm, -10 mm, -20 mm, -30 mm and -40 mm (see Fig. 5)

and 9 for  $-270^\circ$  CA. The RMSs over 15 cycles predicted by the simulations with the coarse and the medium grids show the clear trend of convergence towards the mean flow.

Capturing the correct in-cylinder flow during the intake stroke is essential since the turbulence is generated mainly in this stage and then later affects

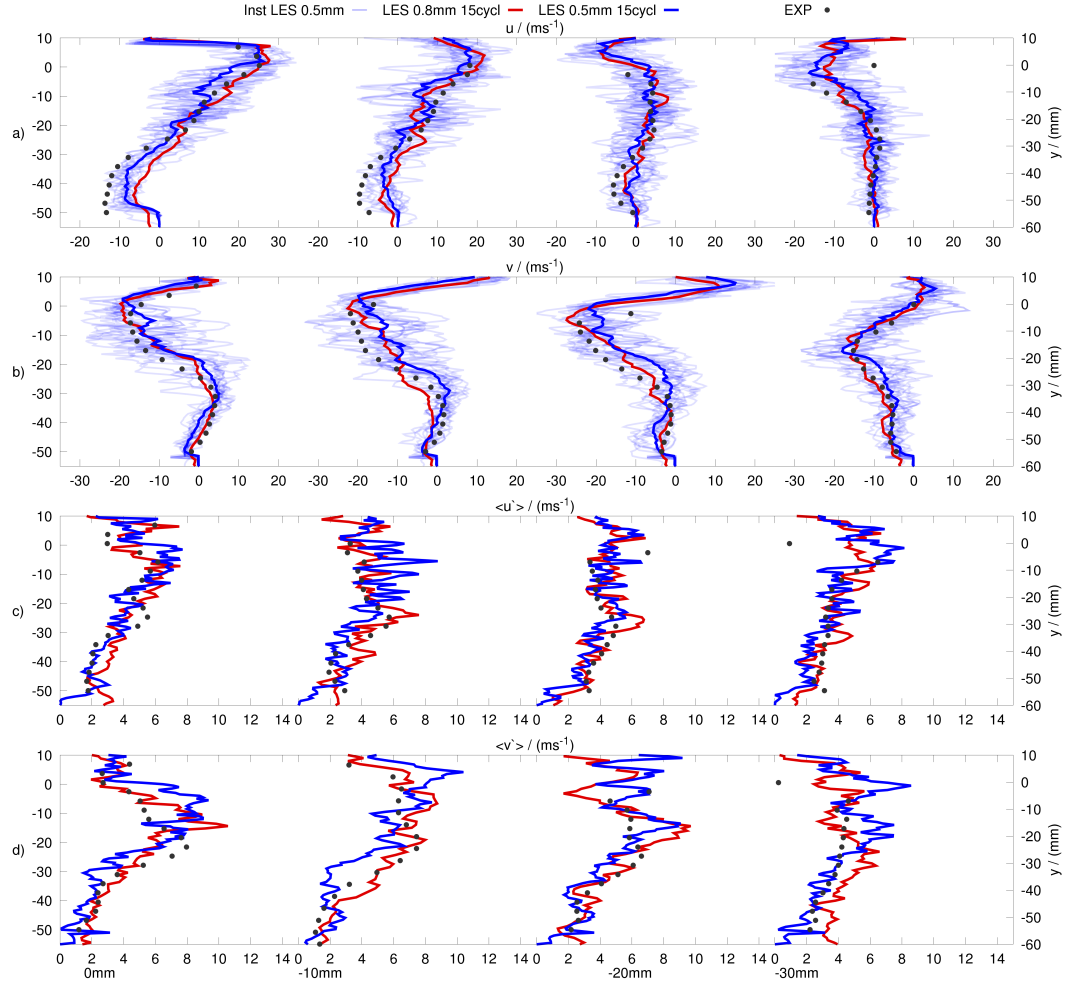


**Fig. 7** Predicted and measured velocity profiles at  $-270^\circ$  CA. Lines in sub-figures (a) and (b) represent the phase averaged horizontal velocity component  $u$  and the vertical velocity component  $v$ . Additionally, 15 instantaneous velocity profiles obtained by the simulation on the medium grid are shown. Sub-figures (c) and (d) illustrate the corresponding RMS of  $u$  and  $v$ , respectively. Experimental results are shown with symbols. Results are shown for the vertical sampling lines at 0 mm, -10 mm, -20 mm and -30 mm (see Fig. 5)

the flame propagation during combustion. However, the valve-overlap in the period between the end of the exhaust stroke and the beginning of the intake stroke creates complicated flow dynamics since the fresh gas and the exhaust gas enter through the intake and the exhaust valves respectively, and interfere with each other. The good agreement found in the comparison between the

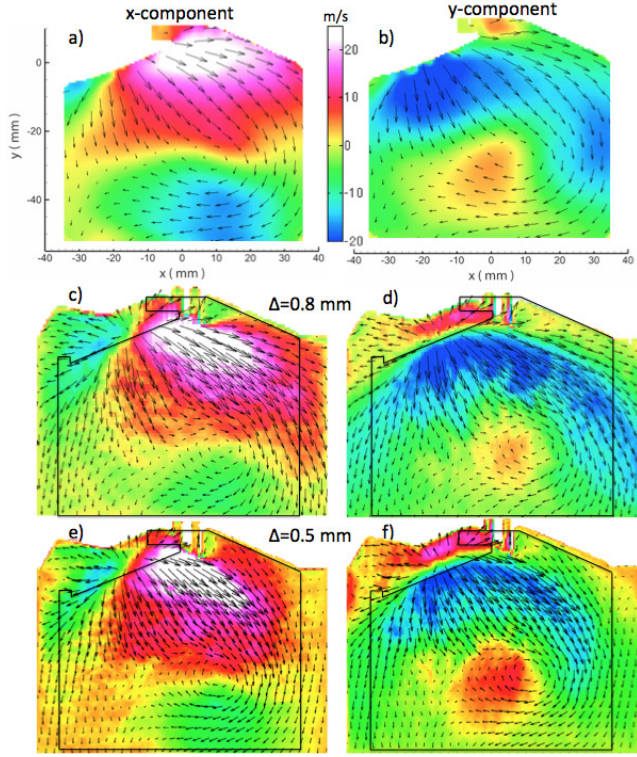


**Fig. 8** Illustration of the phase-averaged velocity components as obtained by the measurement (a,b) and the simulation on the coarse (c,d) and the medium grid (e,f) at  $-270^\circ$  CA

numerical results and the measurement at  $-270^\circ$  CA demonstrates the capability of our proposed approach, with which the complex flow behavior can be well-captured.

Agreement is also achieved for the comparison of the velocity profiles between the simulations and the measurements at  $-90^\circ$  CA during the compression stroke as shown in Figs. 10, 12 and 13.

An overall agreement is achieved at all sampling lines since the flow velocities in the tumble plane are well-captured. Unlike the flow dynamics, which is characterized by high velocity flow due to the pressure difference during the intake stroke, the in-cylinder flow during the compression stroke is driven by the piston motion and the inertia in the flow. Undergoing recirculation, interactions between tumble, eddies, moving walls, and the dissipation of kinetic energy make the dynamics of the flow under compression difficult to predict. Therefore capturing the correct velocity profiles at  $-90^\circ$  CA is a challenging task. Although the numerical results obtained do not fully match the measurements at  $-90^\circ$  CA, the flow velocities are well-predicted for most parts. Unlike the RMSs at  $-270^\circ$  CA, RMSs at  $-90^\circ$  CA show large uncertainty areas

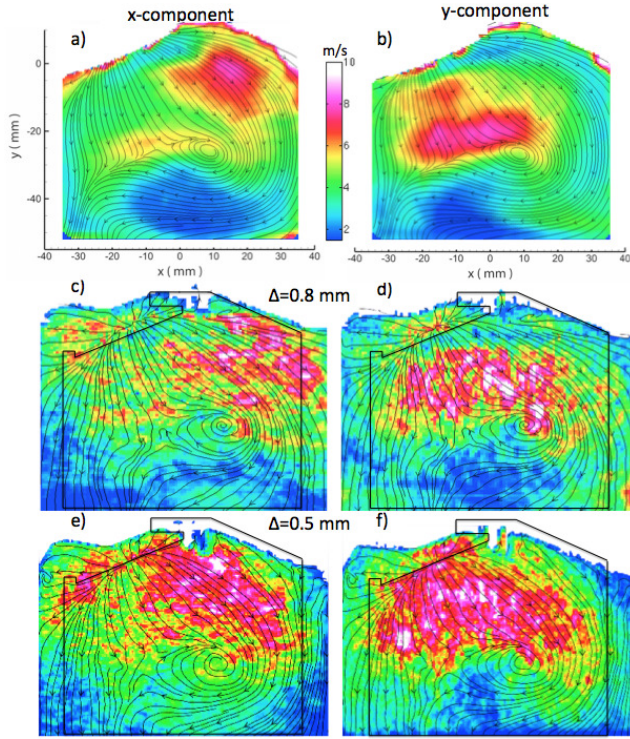


**Fig. 9** The standard deviation for the two measured velocity components at  $-270^\circ$  CA (a,b). The corresponding RMS of the coarse simulation (c,d) ( $\Delta = 0.8 \text{ mm}$ ). The corresponding RMS of the medium simulation (e,f) ( $\Delta = 0.5 \text{ mm}$ )

in the numerical results (Figs. 11c-11f) compared to the measurements (Figs. 11a-11b). Possibly, the flow behavior during compression ( $-90^\circ$  CA) is more sensitive and requires a large number of cycles for converging towards the ensemble mean flow. Another possible reason could be the boundary layer, which is not sufficiently resolved in the near-wall regions. However, according to our experience, the  $\sigma$  model behaves well near walls. Nevertheless, the deviations observed by our simulations are similar to those in the predictions by Baumann et al. [4] where local refinement and wall modeling were employed to resolve the flow near the walls albeit at a lower grid resolution than used by us.

To estimate the convergence of the approach, the RMSs of two velocity components (x and y) at four specific points ( $p_1(0, -40)$ ,  $p_2(0, -10)$ ,  $p_3(30, -15)$ , and  $p_4(-7.5, -17.5) \text{ mm}$ ) in the tumble symmetry plane are plotted as a function of the number of engine cycles. These points are chosen to be consistent with the measurements [3]. As seen in Fig. 14, the convergence rate for the predicted

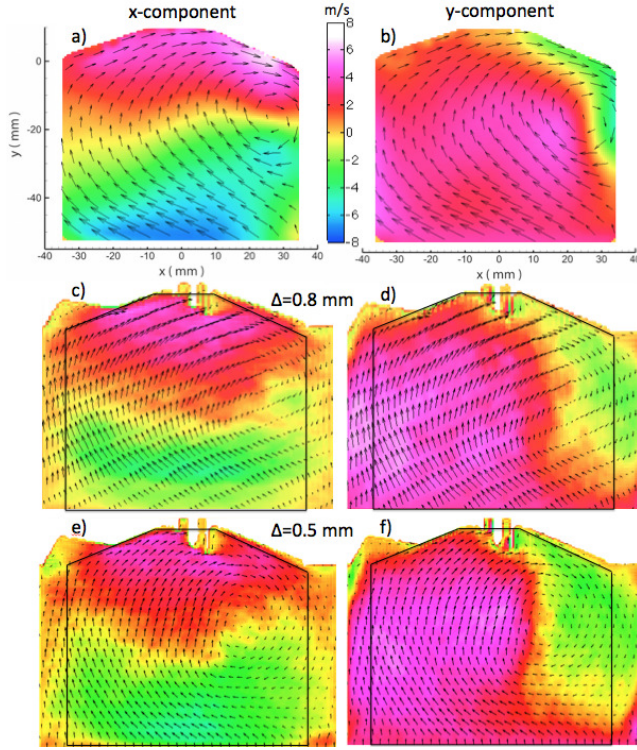


**Fig. 10** Illustration of the phase-averaged velocity components as obtained by the measurement (a,b) and the simulation on the coarse (c,d) and the medium grid (e,f) at  $-90^\circ$  CA

RMS of the coarse and the medium grid is quite visible after 15 simulated cycles.

The in-cylinder pressure curves during intake, compression, expansion and exhaust are compared to the measurements in Fig. 16a. The simulated pressure curves match the measurements well for the motored-case. At TDC, the simulated pressure is 0.5 bar lower than the measured one. This deviation may occur due to the fact that the wall temperature was not measured during the experiments and was assumed to be 400 K in the simulations. Another reason for the low in-cylinder pressure may be the unresolved valve gap (a situation where the valve gap is smaller than one filter or cell size) which allows more gas to escape from the cylinder before IVC. To demonstrate that the mass is conserved inside the cylinder, the trapped mass during compression and expansion is plotted in Fig. 16a\*.

The ratio of turbulent to laminar viscosity may be used as an indicator for regions where the grid is too coarse. Inside the cylinder (Fig. 15), this ratio mostly remains smaller than 10 (Fig. 15a, 15b and 15c) for the medium grid, thus highlighting a good quality of the medium grid [6]. The turbulent

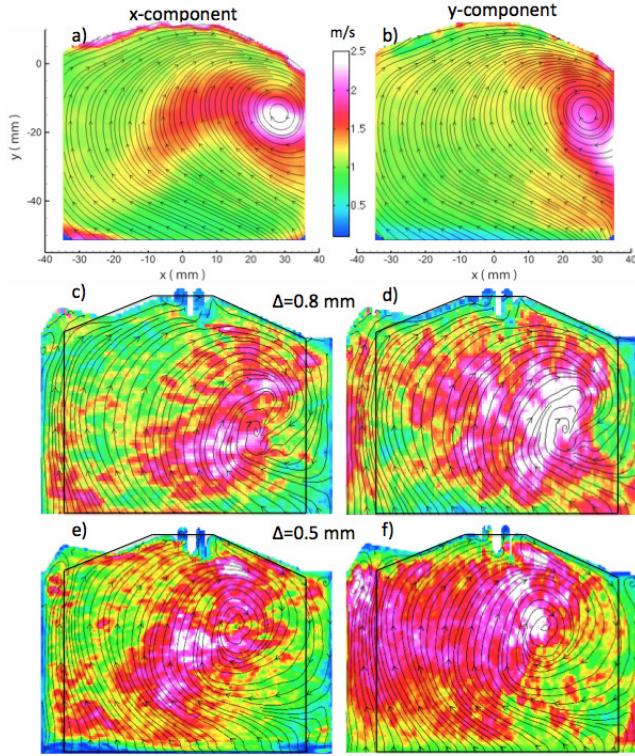


**Fig. 11** The standard deviation for the two measured velocity components at  $-90^\circ$  CA (a,b). The corresponding RMS of the coarse simulation (c,d) ( $\Delta = 0.8\text{mm}$ ). The corresponding RMS of the medium simulation (e,f) ( $\Delta = 0.5\text{mm}$ )

to laminar viscosity ratio exceeds the value of 20 in a small area (Fig. 15d) for the coarse grid. This ratio also shows the thin dissipation layers that are resolved and a high resolution achieved by the LES. It should be stressed that the velocities of the in-cylinder flow reach their maximal values at  $-270^\circ$  CA, which subsequently leads to a large value of the viscosity ratio. In a complete engine cycle, the viscosity ratio for the coarse grid is mostly below a value of 5 (Fig. 15b, Fig. 15c, Fig. 15e, and Fig. 15f), indicating the high quality of even the coarse grid. It should also be noted that comparisons for two different grid resolutions have been presented, showing that the grids are fine enough for the simulations.

### 5.2 Fired-case at 800 rpm

In the fired-case, the predicted pressure curves match the experimental data rather well as it can be seen in Fig. 16b (private communication with Brian Peterson from Darmstadt University). During the expansion stroke, some de-

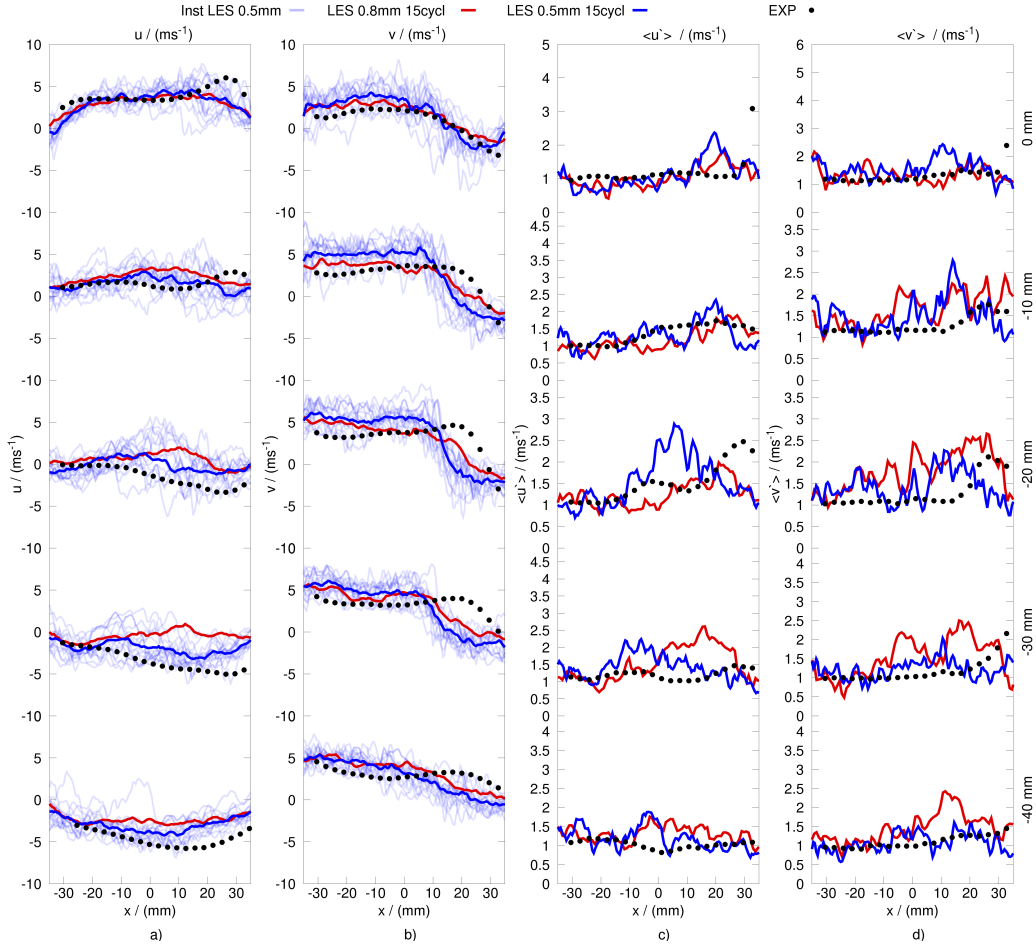


**Fig. 12** Predicted and measured velocity profiles at  $-90^\circ$  CA. Lines in sub-figures (a) and (b) represent the phase averaged horizontal velocity component  $u$  and the vertical velocity component  $v$ . Additionally, 15 instantaneous velocity profiles obtained by the simulation on the medium grid are shown. Sub-figures (c) and (d) illustrate the corresponding RMS of  $u$  and  $v$ , respectively. Experimental results are shown with symbols. Results are shown for the horizontal sampling lines at 0 mm, -10 mm, -20 mm, -30 mm and -40 mm (see Fig. 5)

viations between the simulated and the experimental pressure curves can be seen in Fig. 16b. This discrepancy may be due to the unknown wall temperature, according to our knowledge it is quite sensitive for the combustion case [31, 60]. A further reason may be the neglect of the effect of the unburned gas temperature on the laminar flame speed in the present study, this may

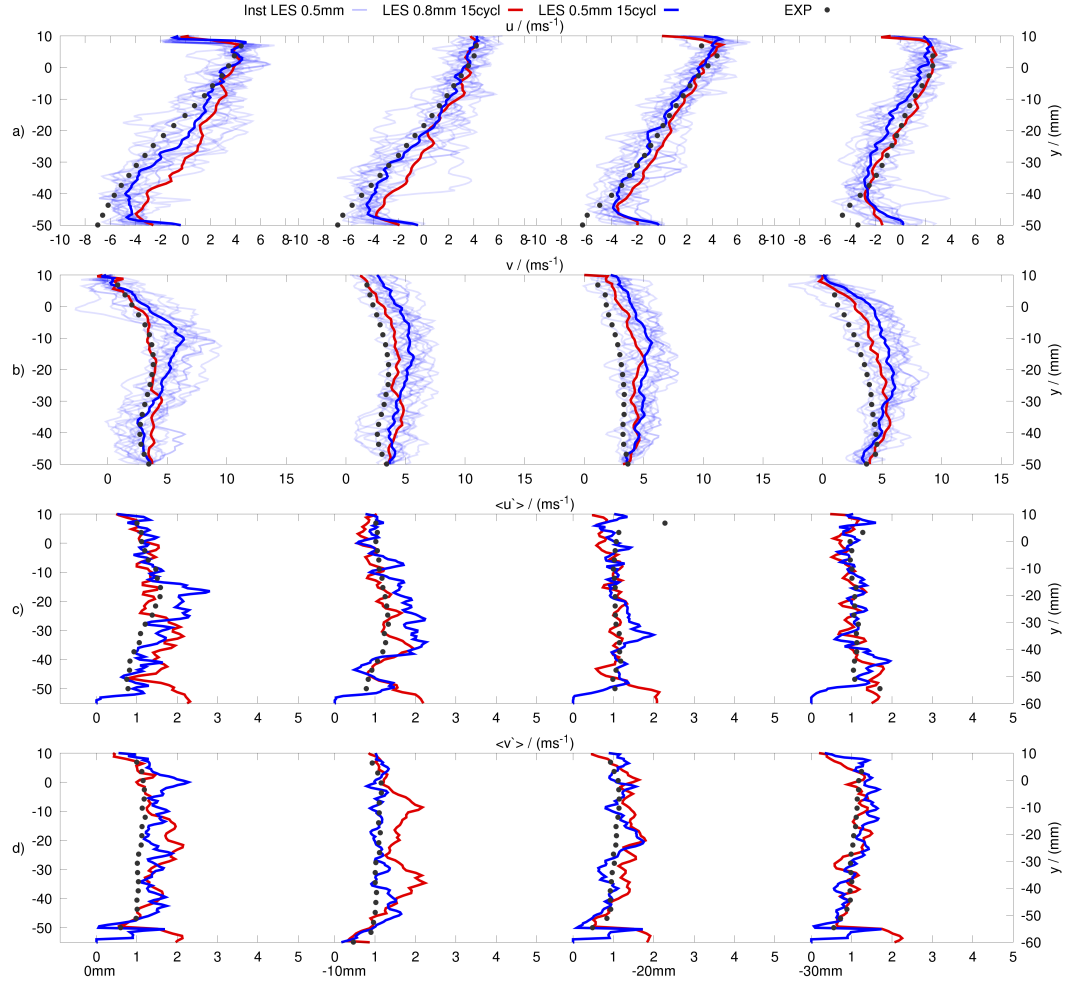


**Fig. 13** Predicted and measured velocity profiles at  $-90^\circ$  CA. Lines in sub-figures (a) and (b) represent the phase averaged horizontal velocity component  $u$  and the vertical velocity component  $v$ . Additionally, 15 instantaneous velocity profiles obtained by the simulation on the medium grid are shown. Sub-figures (c) and (d) illustrate the corresponding RMS of  $u$  and  $v$ , respectively. Experimental results are shown with symbols. Results are shown for the vertical sampling lines at 0 mm, -10 mm, -20 mm and -30 mm (see Fig. 5)

affect the turbulent flame speed as well as the burning duration and lead to the deviation in the pressure curves in Fig. 16b.

A comparison of the simulated and measured flame propagation within a horizontal swirl plane (Fig. 17) is shown in Fig. 18 for different crank angle degrees ( $-6^\circ$  CA to  $4^\circ$  CA). The left side of Fig. 18 shows the flame propagation

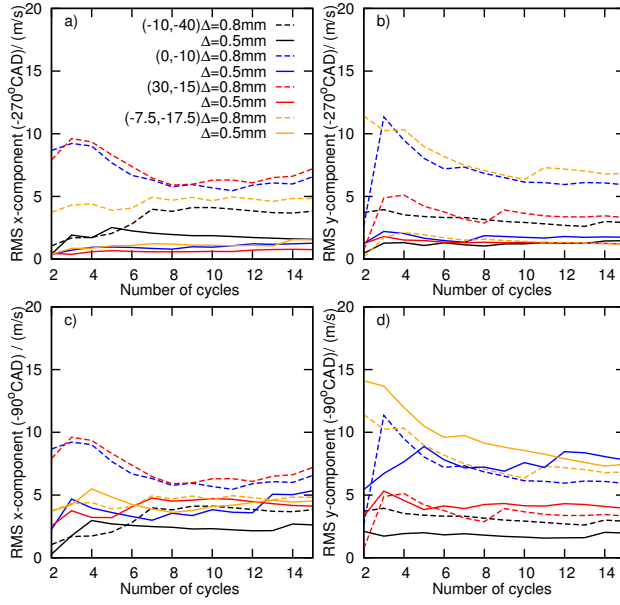


**Fig. 14** The standard deviation in the tumble plane for two grids ( $\Delta = 0.8\text{mm}$  and  $\Delta = 0.5\text{mm}$ ) at  $-270^\circ\text{CA}$  (a,b) and  $-90^\circ\text{CA}$ (c,d). The coordinates of these points are p1(-10,-40), p2(0,-10), p3(30,-15), and p4(-7.5,-17.5) mm

as obtained in the experiments for  $-6^\circ\text{CA}$  to  $4^\circ\text{CA}$  (private communication with Brian Peterson from Darmstadt University). The right side of the figure shows the images of the reaction progress variable source term from the simulation on the medium grid with a cell size of  $\Delta = 0.5\text{ mm}$ . It is found that the general trend of the flame propagation is well-captured, the wrinkles of the flame front in the measurement and the simulation are very similar in structure and scale. This also indicates that the turbulence of the in-cylinder flow is likely to be well-resolved by our approach. The applied FSD model [38] shows a reasonable agreement between the numerical simulation and the measurement for the in-cylinder pressure and the flame propagation.

### 5.3 Numerical results for the motored-case at 1500 RPM

To demonstrate the suitability of the proposed approach for HPC, a fine grid engine simulation was performed on a domain containing 180 million cells with a size of 0.2 mm. Employing 8196 CPUs on the supercomputer JUQUEEN, the computation required around 3.15 million cpu-h to complete a single cycle. Since the simulation is computationally very expensive, only one cycle was computed. We show the coarse and medium cycles' averages combined with the finer results. The fine simulations are not meant to give fully converged statistics but rather additional evidence that a refinement will not change the

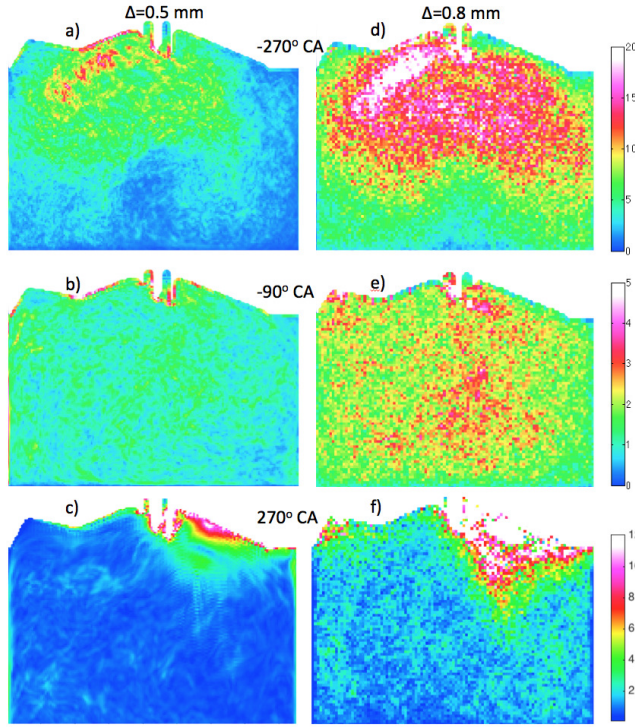


**Fig. 15** The viscosity ratio of turbulent and laminar viscosity ( $\nu_t/\nu$ ) in the tumble plane for the 0.5 mm (a,b,c) and 0.8mm (d,e,f) grid at  $-270^\circ \text{ CA}$ ,  $-90^\circ \text{ CA}$ , and  $270^\circ \text{ CA}$

results much, i.e. that results are largely converged, and give an indication of information that might not be available on a coarse grid. Figures 19 and 22 show the comparison between the simulated instantaneous velocity profiles, 150 measured instantaneous and the corresponding measured mean velocity profiles at  $-270^\circ \text{ CA}$  and  $-90^\circ \text{ CA}$ . A good principal agreement between the measured and simulated velocity structures can be observed as the simulated velocity profiles are well aligned inside the measured velocity profile envelope, the small structures of the flow field are clearly visible. The comparison between the simulated and the measured instantaneous velocities at  $-270^\circ \text{ CA}$  and  $-90^\circ \text{ CA}$  is shown in Figs. 20, 21, 23, and 24. It is interesting to observe that the level of deviation from the ensemble average and the length scales are very consistent (Figs. 23c, 23d, 24c, and 24d). One can also see the high resolution that is achieved by the LES on the 0.2 mm grid compared to the PIV measurements with a resolution of 1.8 mm as given by the experimentalists (Figs. 23 and 24).

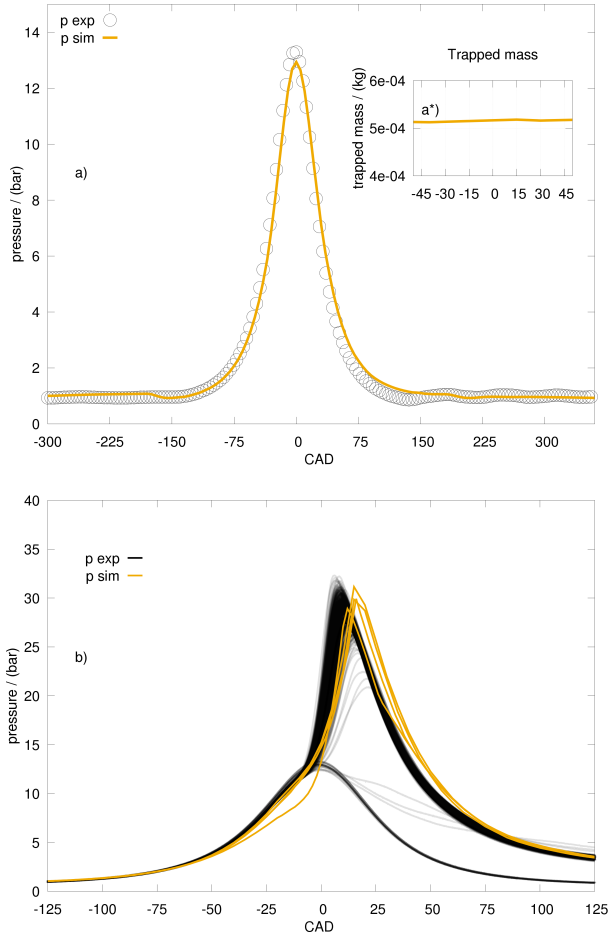


**Fig. 16** Comparison of the in-cylinder pressure obtained from LES simulation without (a) and with (b) combustion against measurements. The mass conservation is illustrated in (a\*) by plotting the trapped mass during compression and expansion.

## 6 Discussion

### 6.1 Numerical efficiency

The presented technique is simple and efficient for engine LES using a particle description of the moving walls. Depending on the resolution of the computational domain, the number of particles that is required for the description of the geometry is different, as shown in Table 5. For a system containing  $N_p$  particles,  $\Theta(N_p)$  operations are required for the numerical treatment, including

solving an ODE for each particle, blocking the particle-containing cells and assigning the velocity and accelerations for the particles. A smaller number of operations, which is usually one order of magnitude lower than  $\Theta(N_p)$ , is applied to impose the flow conditions to the solid cells at the boundaries.

| Test cases                | Number of particles |
|---------------------------|---------------------|
| $\Delta = 0.8 \text{ mm}$ | 73864               |
| $\Delta = 0.5 \text{ mm}$ | 246840              |
| $\Delta = 0.2 \text{ mm}$ | 2988360             |

**Table 5** Number of particles ( $N_p$ ) in different grid sizes

In fact, the number of operations related to the Lagrangian particles is time-dependent, and often not more than 2/3 of the particles are used to handle the moving boundaries. For example, during the intake stroke (after the valve overlap period), the particles describing the exhaust valves are not used. During the compression stroke, the numerical treatments are applied only for the particles describing the piston while both the particles describing the intake and the exhaust valves are not taken part in any numerical operations. Figure 25 shows the number of particles which are used in a complete cycle simulation of a four-stroke engine.

Figure 25 illustrates (for three grid sizes) the ratio of the total number of particles to the number of Eulerian cells (Fig. 25a), the ratio of the number of particles describing the boundaries to the total number of particles (Fig. 25b), and the ratio of used particles to the total number of particles in one cycle of the engine simulation (Fig. 25c). Compared to the total number of numerical operations that are needed for solving the Navier-Stokes equations  $\Theta(N_{\text{cell}})$ , where  $N_{\text{cell}}$  is the number cells of the computational domain, the number of calculations  $\Theta(N_p)$  required by our proposed method is small:  $\Theta(N_p) \subset \Theta(N_{\text{cell}})$ . Additionally, this approach avoids the numerical overhead, and the decomposition of the computational domain is simple and independent from the geometry, while it is efficient in massive parallel simulations (demonstrated using up to 8196 cores). The distributions of the ratio between the number of particles and the number of cells per CPU in one time step in the three test cases are demonstrated in Fig. 26. Obviously, the particles are unequally distributed over the CPUs since the moving boundaries are located in certain areas of the computational domain.

## 6.2 Limitations

Although the proposed approach is simple, flexible, robust, and computational efficient, there are certain limitations that are necessary to be addressed in the scope of this paper.

Firstly, the wall treatment is less than second order accurate (in terms of wall location), which must however be put in perspective to an overall very high grid resolution and the uncertainties involved in the wall modeling of a strong recirculating, highly unsteady flow. Overall, wall treatment is still very much a field of research in IC engine simulations.

Secondly, the major drawback of the proposed method is the limit in resolving the near wall region at fixed and moving boundaries, which may influence the flow and the combustion away from the walls. Obviously, without local refinement, having proper geometric description of the moving surfaces would require more cells, a bigger computational domain and more CPUs. This also leads to a situation when the valve gaps are smaller than the cell/filter size ( $\Delta$ ) and therefore are not resolved. In engine simulation, the description of the "valve lift profile" is crucial to capture the in-cylinder flow processes, as shown by Cleary et al. [9], Davis et al. [10] and Kreuter et al. [30]. Typically, the small valve gap is resolved by a local refinement in the region near the valve seats. However, the importance of resolving the valve gaps down to small value in the range of 0.1-0.125 mm at the beginning of the intake stroke is still questionable. As the intake flow velocity and the piston speed are small, the turbulence that is generated during this short period (10-15 CADs) might not have a strong influence on the overall turbulence of the in-cylinder flow later. It is also questionable whether the relevant turbulence is formed in the valve (seat) boundary layer, which would require a tremendously fine resolution, or rather in the free shear layers downstream of the valve, which requires a good resolution there, while reducing the need for very fine near wall resolution. Nevertheless, further studies on the effect of the small valve gaps on the in-cylinder flow field are necessary to gain better understanding on this issue.

### 6.3 Uniform grid vs. local refinement

The importance of local refinement is undeniable and has been pointed out in the previous sections. However, the uniform Cartesian grid has its own advantages in the LES applications. Classically, one would wish to have the finer resolution near valves while, to compromise with the limited computational resources, the number of cells in the combustion chamber domain must be reduced. Achieving this through increasing the cell size elsewhere leads to artificial dissipation. However with LES, a fine resolution in the combustion chamber and hardly dissipative schemes (e.g. 2nd order central on Cartesian grids) are of paramount importance to avoid artificial dissipation and a too low turbulent flame speeds there. Our paper shows one compromise and what this compromise will result in. We would however like to point out that the compromise of very fine resolution near the valves and a coarse grid in the cylinder is likely to fail with LES, while using very fine grids everywhere is not feasible. A further reason for the artificial or numerical dissipation is a deformation of the cells, such as stretching, compressing or distorting. Moreover, using different cell sizes for the same domain in the LES context causes a

commutation error of  $\mathcal{O}(\Delta^2)$  with the filter width  $\Delta$  (Ghosal et al. [19]). These errors cannot be afforded inside the cylinder, where numerical diffusion would lead to insufficient flame wrinkling, under predicted turbulent flame speed and hence wrong pressure curves and burn out data. Therefore, concentrating the computational effort near the valves and sacrificing the accuracy inside the cylinder may not be a good approach for the LES of an IC engine. Since the in-cylinder flow is driven by inertial forces, pressure difference, and piston motion in a complex geometry, having an equal distribution of computational cells everywhere in the combustion chamber appears to be an appropriate approach to capture the flow dynamics correctly, to resolve a wide range of turbulent scales and to avoid the numerical dissipation. Based on the results obtained on the coarse, medium, and fine meshes, our approach demonstrates the capability of capturing the flow field correctly, even though the smallest valve gap is restricted by the cell size. Our approach, while being very promising with capable computer resources, is computationally costly overall, since a certain "minimum" number of cells is needed to resolve the geometry - so cheap test runs on very coarse grids are not feasible with it. It is however clear that the current progress in computational power is mainly driven by further vectorisation and parallelization, for which our approach is well suited. Table 6 presents the computational costs from different test cases (coarse/medium grids, slow/fast motor speed) of the Darmstadt engine [3]. It becomes clear that the computational costs are reduced significantly when the motor is operated at high RPM. This is a direct result of using a compressible scheme with a small CFL number to resolve acoustic wave propagation - which is often not resolved by less costly simulations.

| Test cases                                  | CPU hours per cycle |
|---|---------------------|
| $\Delta = 0.8 \text{ mm}, 800 \text{ RPM}$  | 4608 cphu/cycle     |
| $\Delta = 0.8 \text{ mm}, 1500 \text{ RPM}$ | 2250 cphu/cycle     |
| $\Delta = 0.5 \text{ mm}, 800 \text{ RPM}$  | 40320 cphu/cycle    |
| $\Delta = 0.5 \text{ mm}, 1500 \text{ RPM}$ | 20160 cphu/cycle    |

**Table 6** Computational cost for different grid sizes and motor speeds

## 7 Conclusions

We have presented the application of LES for simulations of a four-stroke engine with compressible flow, combustion modeling and moving boundaries. The numerical results show a good agreement with the experimental measurements in the case of pure gas exchange, as well as under fired conditions. During pure gas exchange, the flow is driven mainly by the inertia of the fluid flow and the piston and valve motion. The pressure and the velocity profiles

in this operating state show a good agreement with the measurements for all applied grid spacings, which confirms the accuracy and efficiency of the implemented numerical methods. Furthermore, as shown by the numerical results, different grid sizes lead to a very similar amount of the predicted turbulent kinetic energy. This give evidence for the robustness of the applied method.

The simulation of the fired engine showed a well-captured flame propagation. The flame front geometry obtained in the simulation shows a clear similarity to the experiment, similarity in terms of the volume of the flame kernel, its level of corrugation and its propagation speed. The predicted pressure matches the measured pressure of the fired-case. This indicates further the adequateness of the implemented models and the numerical solution, as the flame propagation depends strongly on the turbulence.

The operations describing the particle motion are simple to implement, low in the required number of operations and easy to parallelize - in particular on an isotropic and  $(i, j, k)$ - countable computational grids, where only a few hashing operations are required in order to calculate the logical particle location. The strategy of using Lagrangian particles for describing the moving parts inside the engine was proved to be accurate and of high algorithmic efficiency.

## Acknowledgement

The authors gratefully acknowledge the financial support of the work by the state of North Rhine-Westphalia (NRW), Germany and the computing time granted by the John von Neumann Institute for Computing (NIC) and provided on the supercomputer JUQUEEN at Juelich Supercomputing Centre (JSC). We would like to thank Andreas Dreizler, Elias Baum, Benjamin Böhm from Darmstadt University, and Brian Peterson from Sandia National Labs for their measurements and for many helpful discussions.

## Compliance with Ethical Standards

Conflict of Interest: The authors declare that they have no conflict of interest.

Ethical approval: This article does not contain any studies with human participants or animals performed by any of the authors.

Informed consent: Informed consent was obtained from all individual participants included in the study.

## References

1. Apte, S.V., Gorokhovski, M., Moin, P.: LES of atomizing spray with stochastic modeling of secondary breakup. International Journal of Multiphase Flow **29**(9), 1503–1522 (2003)

2. Balaras, E.: Modeling complex boundaries using an external force field on fixed Cartesian grids in large-eddy simulations. *Computers & Fluids* **33**(3), 375–404 (2004)
3. Baum, E., Peterson, B., Böhm, B., Dreizler, A.: On the validation of LES applied to internal combustion engine flows: Part 1: Comprehensive experimental database. *Flow, Turbulence and Combustion* pp. 1–29 (2013)
4. Baumann, M., di Mare, F., Janicka, J.: On the validation of large eddy simulation applied to internal combustion engine flows part II: Numerical analysis. *Flow, Turbulence and Combustion* **92**(1-2), 299–317 (2014)
5. Boileau, M., Staffelbach, G., Cuenot, B., Poinsot, T., Bérat, C.: LES of an ignition sequence in a gas turbine engine. *Combustion and Flame* **154**(1), 2–22 (2008)
6. Celik, I., Cehreli, Z., Yavuz, I.: Index of resolution quality for large eddy simulations. *Journal of Fluids Engineering* **127**(5), 949–958 (2005)
7. Celik, I., Yavuz, I., Smirnov, A.: Large eddy simulations of in-cylinder turbulence for internal combustion engines: a review. *International Journal of Engine Research* **2**(2), 119–148 (2001)
8. Charlette, F., Meneveau, C., Veynante, D.: A power-law flame wrinkling model for LES of premixed turbulent combustion part I: Non-dynamic formulation and initial tests. *Combustion and Flame* **131**(1), 159–180 (2002)
9. Cleary, D., Silvas, G.: Unthrottled engine operation with variable intake valve lift, duration, and timing. *SAE Technical Paper 2007-01-1282* (2007)
10. Davis, G., Tabaczynski, R., Belaire, R.: The effect of intake valve lift on turbulence intensity and burnrate in SI engines-model versus experiment. *SAE Technical Paper 840030* (1984)
11. Di Mare, F., Jones, W., Menzies, K.: Large eddy simulation of a model gas turbine combustor. *Combustion and Flame* **137**(3), 278–294 (2004)
12. Edge, P., Gubba, S., Ma, L., Porter, R., Pourkashanian, M., Williams, A.: LES modelling of air and oxy-fuel pulverised coal combustionimpact on flame properties. *Proceedings of the Combustion Institute* **33**(2), 2709–2716 (2011)
13. Fadlun, E., Verzicco, R., Orlandi, P., Mohd-Yusof, J.: Combined immersed-boundary finite-difference methods for three-dimensional complex flow simulations. *Journal of Computational Physics* **161**(1), 35–60 (2000)
14. Fansler, T., Drake, M., Böhm, B.: High-speed mie-scattering diagnostics for spray-guided gasoline engine development. In: *Proceedings of the 8th International Symposium on Combustion Diagnostics*, Baden-Baden, pp. 413–425 (2008)
15. Fontanesi, S., Paltrinieri, S., D'Adamo, A., Cantore, G., Rutland, C.: Knock tendency prediction in a high performance engine using LES and tabulated chemistry. *SAE International Journal of Fuels and Lubricants* **6**(1), 98–118 (2013)
16. Forrer, H., Berger, M.: Flow simulations on Cartesian grids involving complex moving geometries. In: *Hyperbolic problems: theory, numerics, ap-*

- plications, pp. 315–324. Springer (1999)
- 17. Franchetti, B., Marincola, F.C., Navarro-Martinez, S., Kempf, A.: Large eddy simulation of a pulverised coal jet flame. *Proceedings of the Combustion Institute* **34**(2), 2419–2426 (2013)
  - 18. Fureby, C.: A fractal flame-wrinkling large eddy simulation model for premixed turbulent combustion. *Proceedings of the Combustion Institute* **30**(1), 593 – 601 (2005)
  - 19. Ghosal, S., Moin, P.: The basic equations for the large eddy simulation of turbulent flows in complex geometry. *Journal of Computational Physics* **118**(1), 24–37 (1995)
  - 20. Goldstein, D., Handler, R., Sirovich, L.: Direct numerical simulation of turbulent flow over a modeled riblet covered surface. *Journal of Fluid Mechanics* **302**, 333–376 (1995)
  - 21. Goryntsev, D., Sadiki, A., Klein, M., Janicka, J.: Large eddy simulation based analysis of the effects of cycle-to-cycle variations on air–fuel mixing in realistic DISI IC-engines. *Proceedings of the Combustion Institute* **32**(2), 2759–2766 (2009)
  - 22. Gourdain, N., Gicquel, L., Montagnac, M., Vermorel, O., Gazaix, M., Staffelbach, G., Garcia, M., Boussuge, J., Poinsot, T.: High performance parallel computing of flows in complex geometries: I. methods. *Computational Science & Discovery* **2**(1), 015,003 (2009)
  - 23. Haworth, D., Jansen, K.: Large-eddy simulation on unstructured deforming meshes: towards reciprocating IC engines. *Computers & fluids* **29**(5), 493–524 (2000)
  - 24. Heywood, J.B.: Internal combustion engine fundamentals, vol. 930. McGraw-Hill New York (1988)
  - 25. Hirt, C., Amsden, A.A., Cook, J.: An arbitrary Lagrangian-Eulerian computing method for all flow speeds. *Journal of Computational Physics* **14**(3), 227–253 (1974)
  - 26. Kempf, A., Geurts, B., Oefelein, J.: Error analysis of large-eddy simulation of the turbulent non-premixed sydney bluff-body flame. *Combustion and Flame* **158**(12), 2408–2419 (2011)
  - 27. Kempf, A., Klein, M., Janicka, J.: Efficient generation of initial-and inflow-conditions for transient turbulent flows in arbitrary geometries. *Flow, Turbulence and combustion* **74**(1), 67–84 (2005)
  - 28. Kempf, A., Lindstedt, R., Janicka, J.: Large-eddy simulation of a bluff-body stabilized nonpremixed flame. *Combustion and flame* **144**(1), 170–189 (2006)
  - 29. Kim, W.W., Menon, S., Mongia, H.C.: Large-eddy simulation of a gas turbine combustor flow. *Combustion Science and Technology* **143**(1-6), 25–62 (1999)
  - 30. Kreuter, P., Heuser, P., Schebitz, M.: Strategies to improve SI-engine performance by means of variable intake lift, timing and duration. *SAE Technical Paper 920449* (1992)
  - 31. Luo, X., Yu, X., Zha, K., Jansons, M., Soloiu, V.: In-cylinder wall temperature influence on unburned hydrocarbon emissions during transitional

- period in an optical engine using a laser-induced phosphorescence technique. *SAE International Journal of Engines* **7**(2014-01-1373), 995–1002 (2014)
- 32. Ma, T., Stein, O., Chakraborty, N., Kempf, A.: A posteriori testing of algebraic flame surface density models for LES. *Combustion Theory and Modelling* **17**(3), 431–482 (2013)
  - 33. Mittal, R., Iaccarino, G.: Immersed boundary methods. *Annual Review of Fluid Mechanics* **37**, 239–261 (2005)
  - 34. Mittal, V., Kang, S., Doran, E., Cook, D., Pitsch, H.: LES of gas exchange in IC engines. *Oil & Gas Science and Technology–Revue d’Energies nouvelles* **69**(1), 29–40 (2014)
  - 35. Mohd-Yusof, J.: Combined immersed-boundary/B-spline methods for simulations of flow in complex geometries. *Annual Research Briefs. NASA Ames Research Center, Stanford University Center of Turbulence Research: Stanford* pp. 317–327 (1997)
  - 36. Morse, A., Whitelaw, J., Yianneskis, M.: Turbulent flow measurements by laser doppler anemometry in a motored reciprocating engine. *Imperial College Mechanical Engineering Department Report FS/78/24* (1978)
  - 37. Moureau, V., Domingo, P., Vervisch, L.: From large-eddy simulation to direct numerical simulation of a lean premixed swirl flame: Filtered laminar flame-pdf modeling. *Combustion and Flame* **158**(7), 1340–1357 (2011)
  - 38. Muppala, S., Aluri, N.K., Dinkelacker, F., Leipertz, A.: Development of an algebraic reaction rate closure for the numerical calculation of turbulent premixed methane, ethylene, and propane/air flames for pressures up to 1.0 mpa. *Combustion and flame* **140**(4), 257–266 (2005)
  - 39. Nguyen, T., Janas, P., Lucchini, T., D’Errico, G., Kaiser, S., Kempf, A.: LES of flow processes in an SI engine using two approaches: Openfoam and PsiPhi. *SAE Technical Paper 2014-01-1121* (2014)
  - 40. Nicoud, F., Toda, H.B., Cabrit, O., Bose, S., Lee, J.: Using singular values to build a subgrid-scale model for large eddy simulations. *Physics of Fluids* **23**(8), 085,106 (2011)
  - 41. Peskin, C.S.: Flow patterns around heart valves: a numerical method. *Journal of Computational Physics* **10**(2), 252–271 (1972)
  - 42. Pettit, M., Coriton, B., Gomez, A., Kempf, A.: Large-eddy simulation and experiments on non-premixed highly turbulent opposed jet flows. *Proceedings of the Combustion Institute* **33**(1), 1391–1399 (2011)
  - 43. Pierce, C.D., Moin, P.: Progress-variable approach for large-eddy simulation of non-premixed turbulent combustion. *Journal of Fluid Mechanics* **504**, 73–97 (2004)
  - 44. Pitsch, H.: Large-eddy simulation of turbulent combustion. *Annual Review of Fluid Mechanics* **38**, 453–482 (2006)
  - 45. Poinsot, T., Veynante, D.: *Theoretical and numerical combustion*. RT Edwards Inc. (2005)
  - 46. Poinsot, T.J., Lele, S.: Boundary conditions for direct simulations of compressible viscous flows. *Journal of computational physics* **101**(1), 104–129 (1992)

47. Proch, F., Kempf, A.: Modeling heat loss effects in the large eddy simulation of a model gas turbine combustor with premixed flamelet generated manifolds. *Proceedings of the Combustion Institute* **35**(3), 3337–3345 (2015)
48. Richard, S., Colin, O., Vermorel, O., Benkenida, A., Angelberger, C., Veynante, D.: Towards large eddy simulation of combustion in spark ignition engines. *Proceedings of the Combustion Institute* **31**(2), 3059–3066 (2007)
49. Rieth, M., Proch, F., Stein, O., Pettit, M., Kempf, A.: Comparison of the Sigma and Smagorinsky LES models for grid generated turbulence and a channel flow. *Computers & Fluids* **99**, 172–181 (2014)
50. Rittler, A., Proch, F., Kempf, A.M.: LES of the sydney piloted spray flame series with the PFGM/ATF approach and different sub-filter models. *Combustion and Flame* **162**(4), 1575–1598 (2015)
51. Sankaran, V., Menon, S.: LES of spray combustion in swirling flows\*. *Journal of Turbulence* **3**(11), 1–23 (2002)
52. Sone, K., Patel, N., Menon, S.: Large eddy simulation of fuel-air mixing in an internal combustion engine. *AIAA paper* **635** (2001)
53. Taira, K., Colonius, T.: The immersed boundary method: a projection approach. *Journal of Computational Physics* **225**(2), 2118–2137 (2007)
54. de Tullio, M.D., De Palma, P., Iaccarino, G., Pascazio, G., Napolitano, M.: An immersed boundary method for compressible flows using local grid refinement. *Journal of Computational Physics* **225**(2), 2098–2117 (2007)
55. Turns, S.R.: An introduction to combustion. 2nd (2000)
56. Udaykumar, H., Mittal, R., Rampunggoon, P., Khanna, A.: A sharp interface Cartesian grid method for simulating flows with complex moving boundaries. *Journal of Computational Physics* **174**(1), 345–380 (2001)
57. Udaykumar, H., Shyy, W., Rao, M.: Elafint: a mixed Eulerian–Lagrangian method for fluid flows with complex and moving boundaries. *International journal for numerical methods in fluids* **22**(8), 691–712 (1996)
58. Vermorel, O., Richard, S., Colin, O., Angelberger, C., Benkenida, A., Veynante, D.: Towards the understanding of cyclic variability in a spark ignited engine using multi-cycle LES. *Combustion and Flame* **156**(8), 1525–1541 (2009)
59. Verzicco, R., Mohd-Yusof, J., Orlandi, P., Haworth, D.: LES in complex geometries using boundary body forces. *Center for Turbulence Research Proceedings of the Summer Program, NASA Ames and Stanford University* pp. 171–186 (1998)
60. Wilhelmsson, C., Vressner, A., Tunestål, P., Johansson, B., Särner, G., Aldén, M.: Combustion chamber wall temperature measurement and modeling during transient HCCI operation. *SAE Technical Papers* 2005-01-3731 (2005)
61. Wu, H.W., Perng, S.W.: LES analysis of turbulent flow and heat transfer in motored engines with various SGS models. *International journal of heat and mass transfer* **45**(11), 2315–2328 (2002)
62. Wyngaard, J.: Atmospheric turbulence. *Annual Review of Fluid Mechanics* **24**(1), 205–234 (1992)

- 
- 63. Zhou, G.: Numerical simulations of physical discontinuities in single and multi-fluid flows for arbitrary Mach numbers. Chalmers University of Technology, (1995)
  - 64. Zhou, H., Flamant, G., Gauthier, D.: DEM-LES simulation of coal combustion in a bubbling fluidized bed part II: coal combustion at the particle level. *Chemical Engineering Science* **59**(20), 4205–4215 (2004)

## Appendix A Simplified engine with fixed axisymmetric valve

The simulated engine [3] provides a realistic but very complex test case for our simulation results. A much simpler experiment was conducted in a classic work by Morse and Whitelaw [36], which is commonly used as a bench mark for groups developing techniques for engine simulation. (Since we have no access to the original report of Morse and Whitelaw, the measurement data was taken from the paper of Verzicco et al. [59].) This appendix presents our results of this testcase for the sake of completeness. The engine geometry is characterized by a fixed central valve, which allows the fluid to flow through the 4 mm-wide annular gap between the valve and the cylinder head. The piston motion is described by a harmonic function (Eq. 25) as shown below:

$$z_p = s_1 + \frac{s}{2} \cos(\omega t) \quad (25)$$

The detailed information about the parameters and the engine configuration are given in Fig. A.1: In the experiment, the engine is motored at a speed of 200RPM (21 rad/s) with a Reynolds number of 2000. Since the mean piston velocity is considered to be small ( $\bar{V}_p = 0.4$  m/s), the computation will take a long time with a compressible solver. To reduce the cost for the simulation, the engine speed and the molecular viscosity were increased by a factor of 10, maintaining Reynolds similarity.

Five cycles were simulated on a 7.9 million cell-domain for a cell size of 0.5 mm. Using 240 CPUs, it took 85 hours to complete one cycle (360° Crank angle degree). The results are sampled at 36° CA and 144° CA after TDC for three sampling lines (Fig. A.1). A Good agreement is achieved between the simulation results and the experimental data for both the velocity profiles and the RMS.

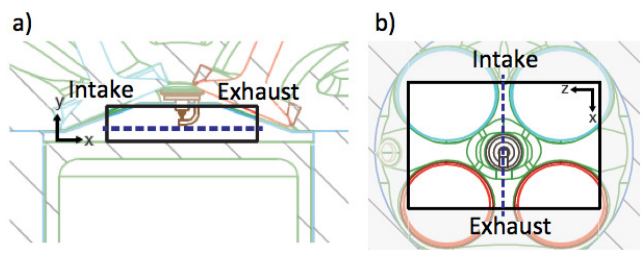


**Fig. 17** The vertical position of the interrogation window (a) and the size of the interrogation region (b) (private communication with Brian Peterson from Darmstadt University)

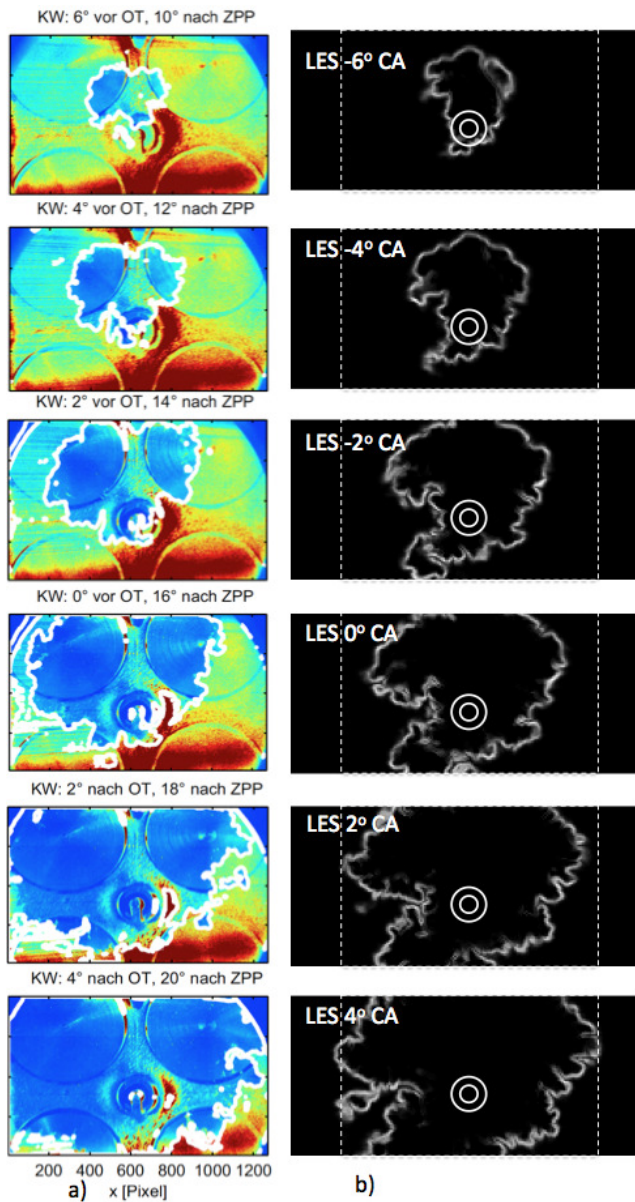


**Fig. 18** Images of the flame propagation within a horizontal swirl plane (Fig. 17) from (a) the experiment (view from the top of the engine, the two intake ports are shown in the upper part of the image, and the two exhaust ports are in the lower part ) (private communication with Brian Peterson from Darmstadt University) and (b) the simulation ( $\Delta = 0.5$  mm)

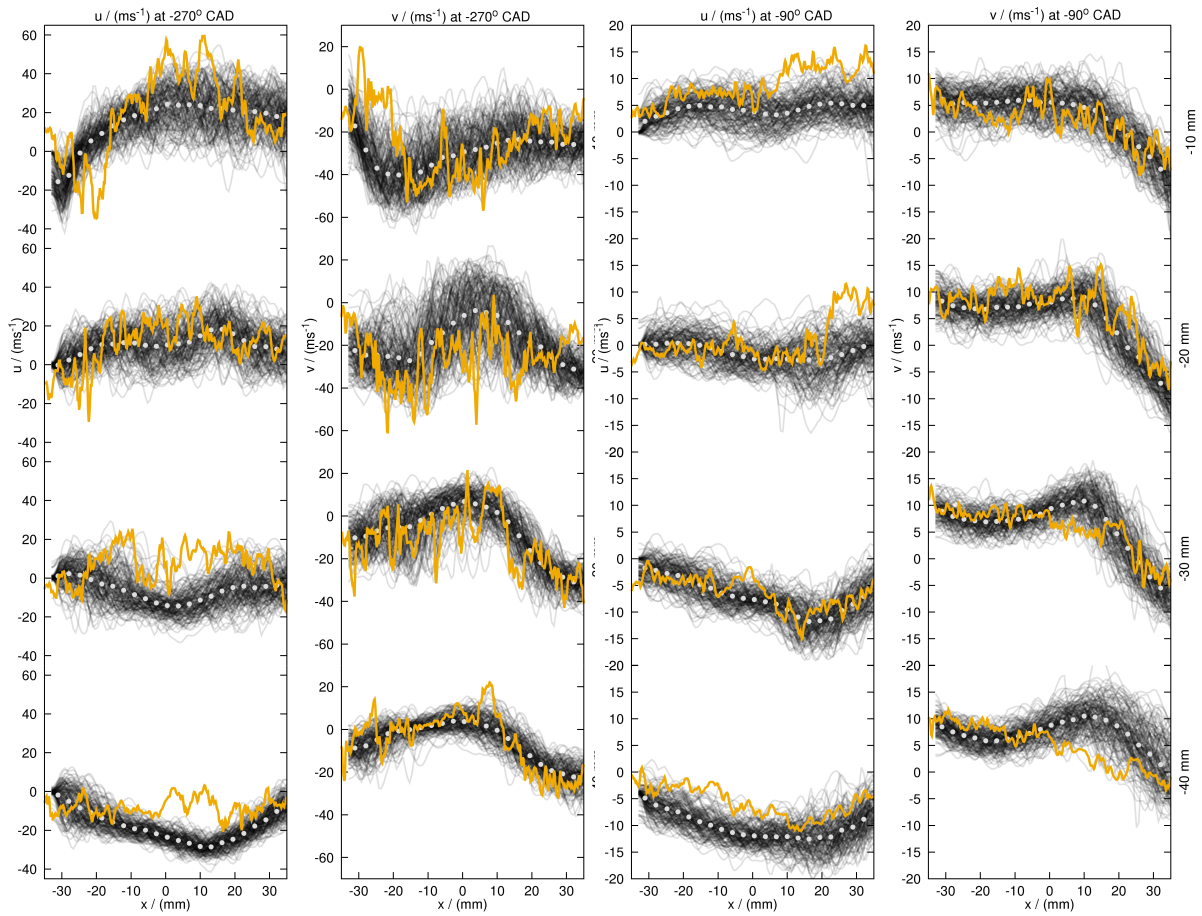


**Fig. 19** Velocity profiles obtained on the fine grid; measured instantaneous (—), measured mean (○) and simulated (—) on the fine grid. The results are shown for the horizontal sampling lines at -10mm, -20mm, -30mm and -40mm (see Fig. 5)

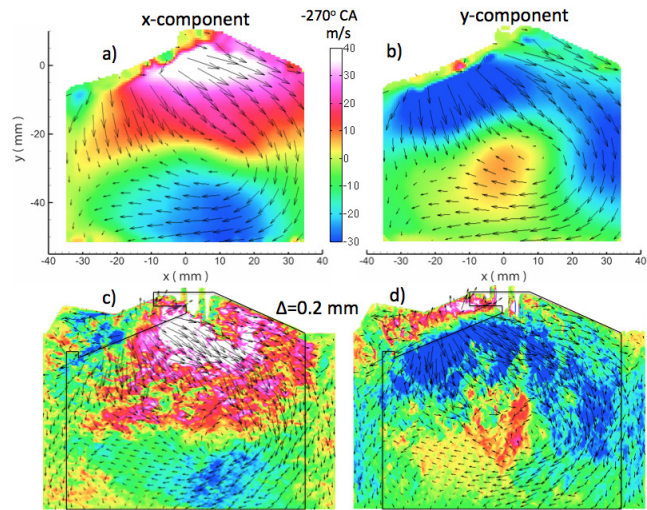


**Fig. 20** The phase-averaged measured (a,b) and the instantaneous simulated (c,d) velocity components obtained on the fine grid at  $-270^\circ$ CA

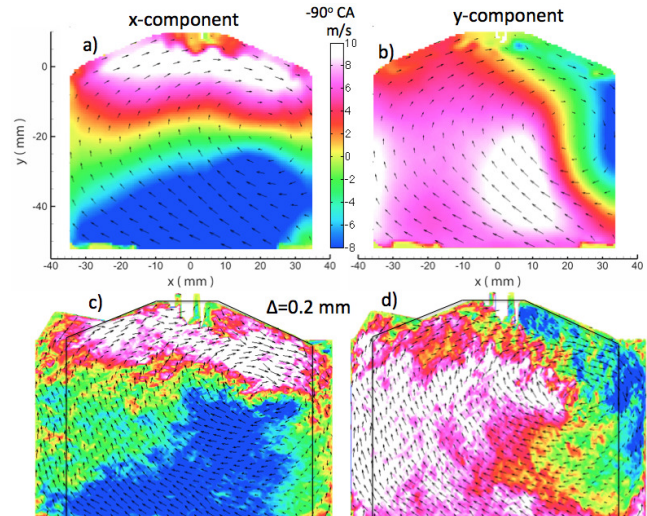


**Fig. 21** The phase-averaged measured (a,b) and the instantaneous simulated (c,d) velocity components obtained on the fine grid at  $-90^\circ$ CA

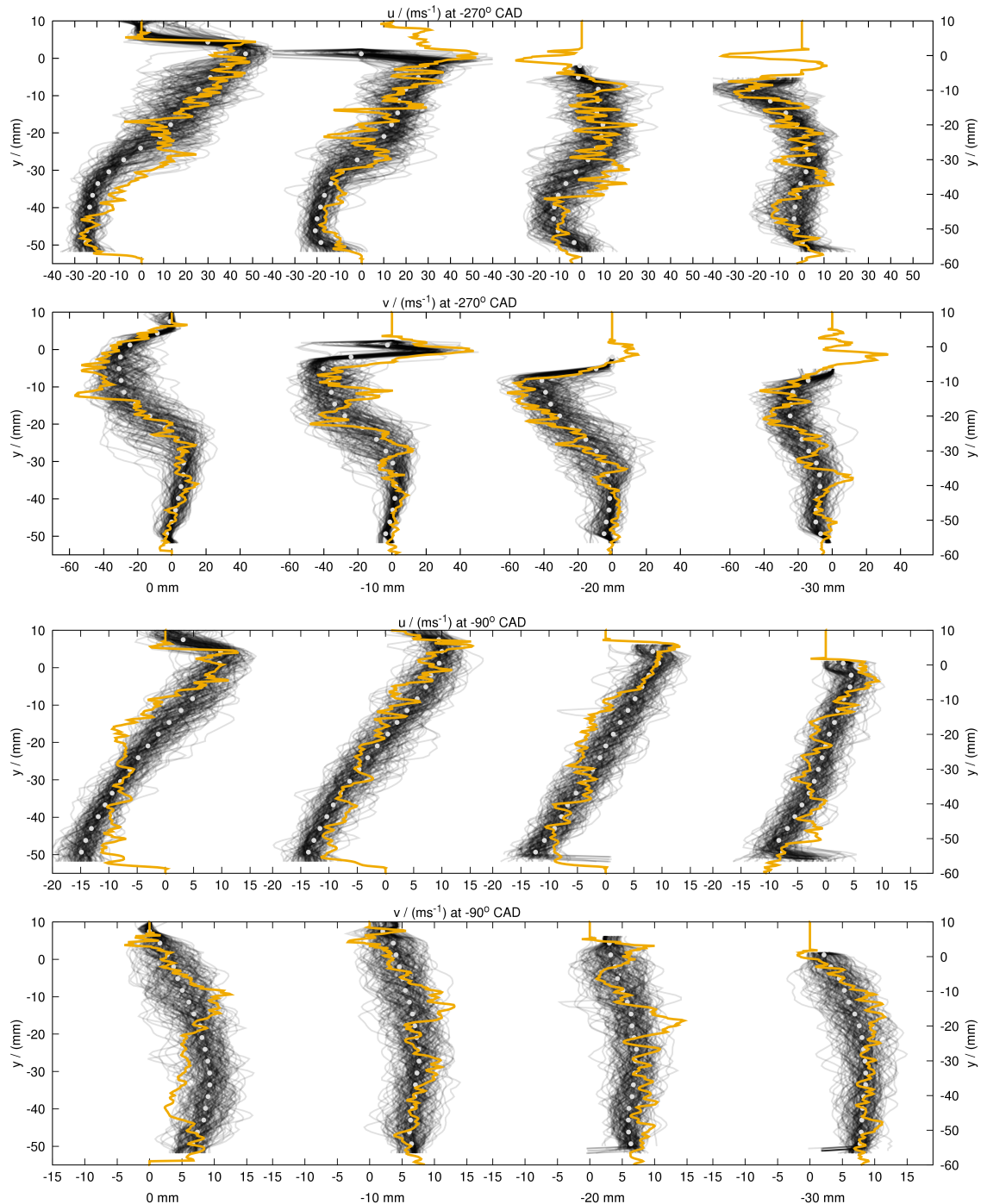


**Fig. 22** Velocity profiles obtained on the fine grid; measured instantaneous (—), measured mean ( $\circ$ ) and simulated (—) on the fine grid. The results are shown for the vertical sampling lines at 0 mm, -10 mm, -20 mm and -30 mm (see Fig. 5)

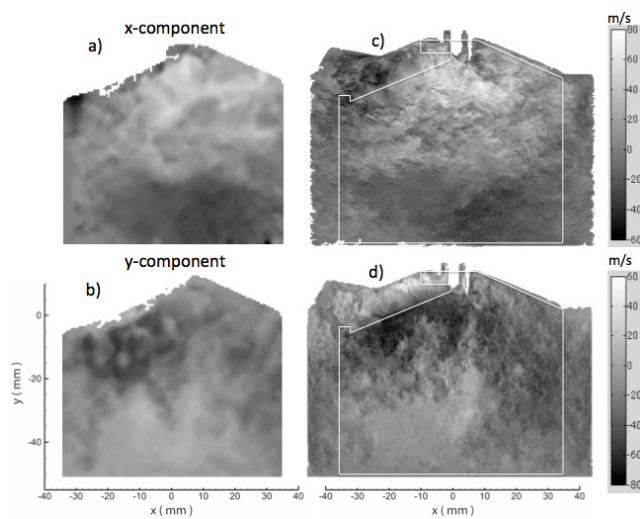


**Fig. 23** The instantaneous measured horizontal (a) and vertical (b) velocity components at  $-270^\circ\text{CA}$ . The corresponding simulated instantaneous velocity components (c,d) were obtained on the fine grid

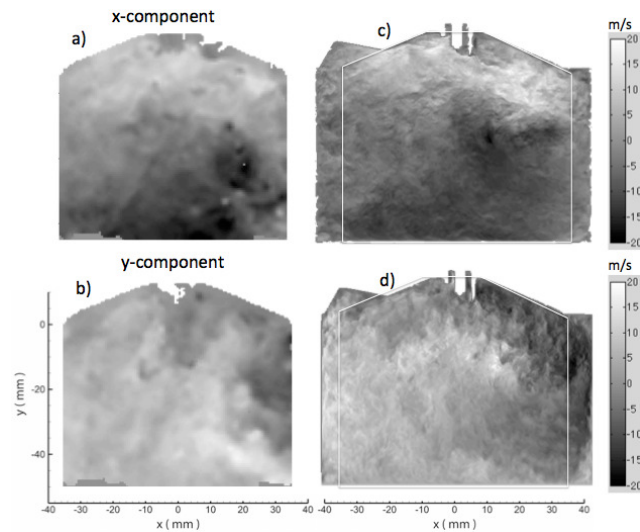


**Fig. 24** The instantaneous measured horizontal (a) and vertical (b) velocity components at  $-90^\circ\text{CA}$ . The corresponding simulated instantaneous velocity components (c,d) were obtained on the fine grid

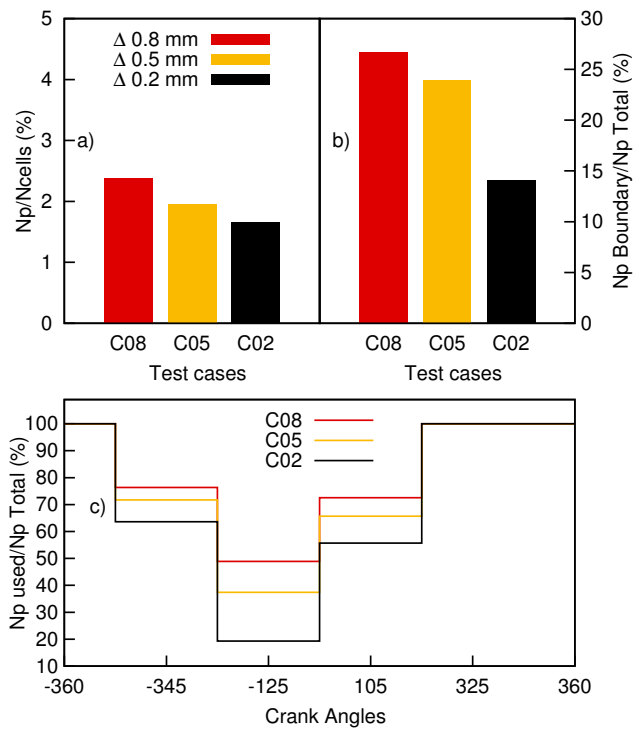


**Fig. 25** Ratio of the total number of particles ( $N_{pt}$ ) to the total number of computational cells ( $N_c$ ) (a). Ratio of the number of boundary particles ( $N_{pb}$ ) to the total number of particles (b). Percentage of the used particles ( $N_{pu}$ ) over a complete engine cycle simulation (c)

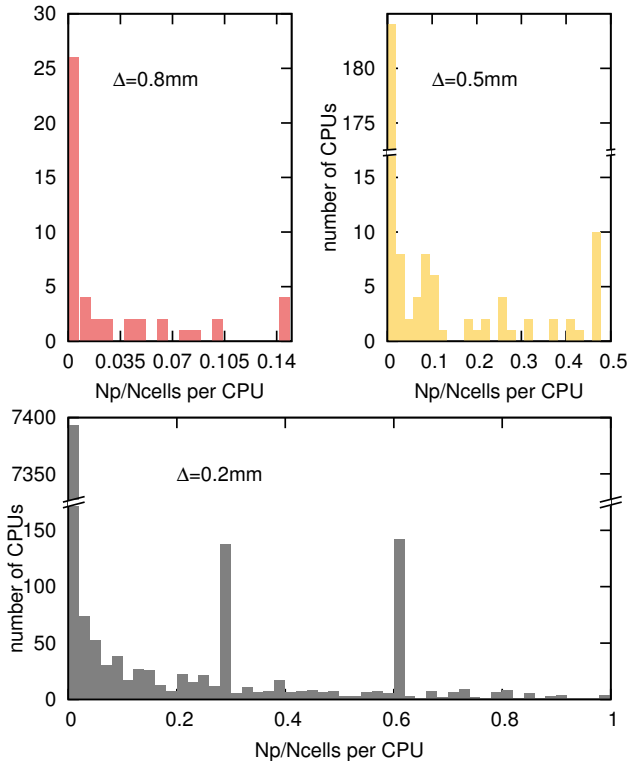


**Fig. 26** The distribution of the ratio of the number of particles ( $N_p$ ) to the number of cells ( $N_{\text{cell}}$ ) per CPU in the three test cases.

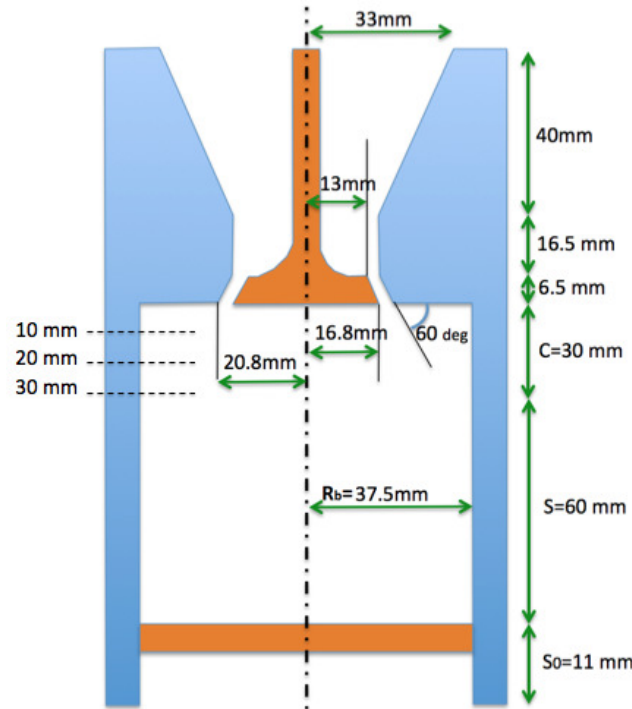


**Fig. A.1** Engine geometry with three sampling lines at 10 mm, 20 mm, and 30 mm below the central valve (Morse et al. [36])

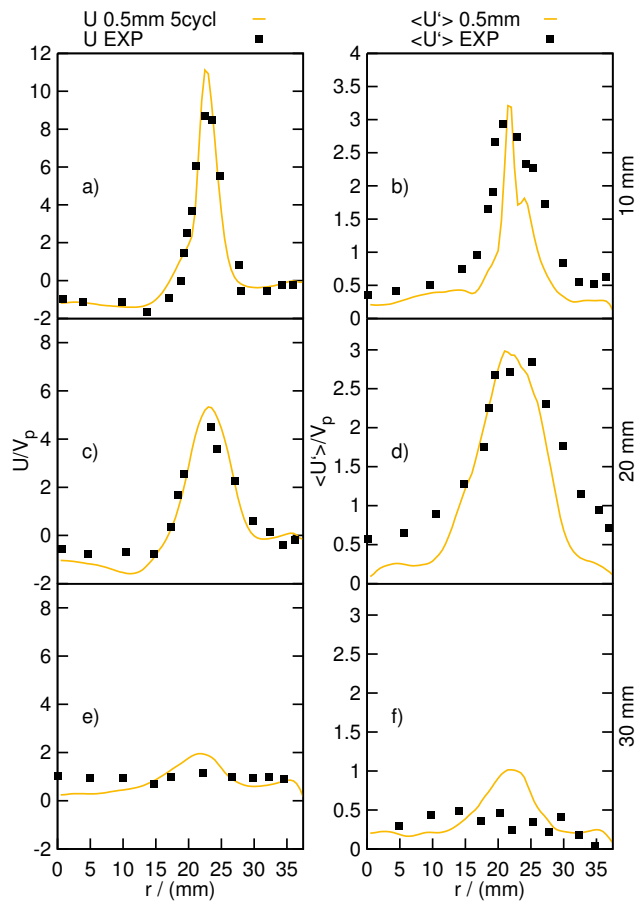


**Fig. A.2** Predicted and measured velocity profiles at 36° CA: Vertical velocity at 10 mm (a), 20 mm (c) and 30 mm (e). The corresponding RMS at 10 mm (b), 20 mm (d) and 30 mm (f)

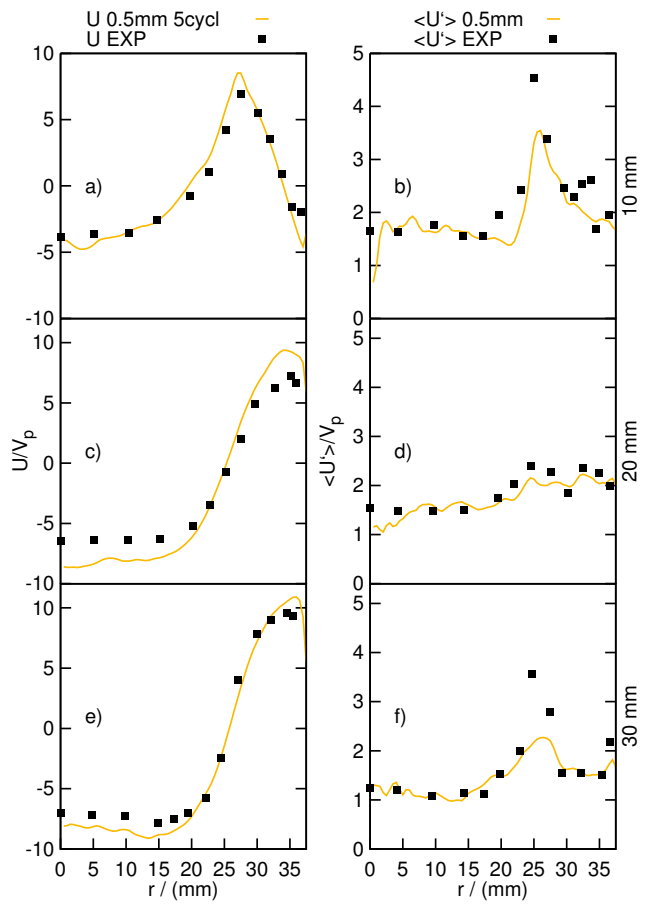


**Fig. A.3** Predicted and measured velocity profiles at  $144^\circ$  CA: Vertical velocity at 10 mm (a), 20 mm (c) and 30 mm (e). The corresponding RMS at 10 mm (b), 20 mm (d) and 30 mm (f)